Molybdenum Sulfide Clusters as Molecular Co-Catalyst on Antimony Selenide Photocathodes for Photoelectrochemical Hydrogen Evolution

Pardis Adams[†], Jan Bühler[†], Iva Walz[†], Thomas Moehl[†], Helena Roithmeyer[†], Olivier Blacque[†], Nicolò Comini[‡§], J. Trey Diulus[‡§], Roger Alberto[†], Sebastian Siol[‖], Mirjana Dimitrievska[‖], Zbynek Novotny[‡§], and S. David Tilley[†]**

[†] Department of Chemistry, University of Zurich, Winterthurerstrasse 190, Zurich, 8057, Switzerland

[‡] Department of Physics, University of Zurich, Winterthurerstrasse 190, Zurich, 8057, Switzerland

[§] Swiss Light Source, Paul Scherrer Institute, Villigen-PSI, Switzerland

[‖] Surface Science and Coating Technologies Laboratory/ Transport at Nanoscale Interfaces Laboratory, Swiss Federal Laboratories for Materials Science and Technology (EMPA), Ueberlandstrasse 129, Dübendorf, 8600, Switzerland

Corresponding Author

S. David Tilley – Department of Chemistry, University of Zurich, Winterthurerstrasse 190, Zurich, 8057, Switzerland, E-mail: david.tilley@chem.uzh.ch

Zbynek Novotny – Department of Physics, University of Zurich, Winterthurerstrasse 190, Zurich, 8057, Switzerland, E-mail: zbynek.novotny@pnnl.gov

Molybdenum sulfide serves as an effective non-precious metal catalyst for hydrogen evolution, primarily active at edge sites with unsaturated molybdenum sites or terminal disulphides. To improve the activity at low loading density, two molybdenum sulfide clusters, $[Mo_3S_4]^{4+}$ and $[Mo_3S_{13}]^{2-}$, were investigated. The Mo_3S_x molecular catalysts were heterogenized on Sb_2Se_3 with a simple soaking treatment, resulting in a thin catalyst layer of only a few nanometers that gave up to 20 mA cm^{-2} under one sun illumination. Both $[Mo_3S_4]^{4+}$ and $[Mo_3S_{13}]^{2-}$ exhibit catalytic activities on Sb_2Se_3 through a simple soaking process, with $[Mo_3S_{13}]^{2-}$ emerging as the superior catalyst, demonstrating enhanced photovoltage and average faradaic efficiency of 100% for hydrogen evolution. This superiority is attributed to the effective loading and higher catalytic activity of $[Mo_3S_{13}]^{2-}$ on the Sb_2Se_3 surface, validated by X-ray photoelectron and Raman spectroscopy.

TOC GRAPHICS

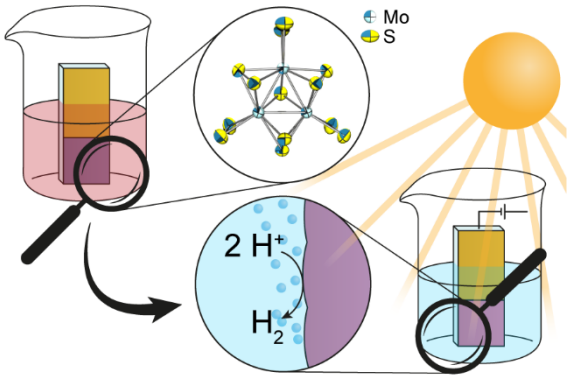

Rising temperatures and climate variations strain natural and human systems, while an increasing energy gap, heightened by geopolitical tensions, prompts a global shift towards greener energy;[1,2] however, the limited adoption of renewable sources, particularly in hydrogen production, underscores the need to explore alternative methods like emerging photoelectrochemical water-splitting technologies.[3,4] Antimony selenide (Sb_2Se_3) garnered attention for solar water splitting, due to its promising characteristics, including a high absorption coefficient ($>10^5$ cm^{-1}), photostability, and cost-effective obtainment and synthesis.[5–10] This material shows excellent performance and stability when paired with suitable catalysts. Therefore, the search for active, easy-to-prepare, and versatile catalysts is an essential factor for the long-term success of this material. While platinum is the most commonly used catalyst for the hydrogen evolution reaction (HER) due to its high catalytic activity and minimal overpotential, its scarcity and high cost hinder large-scale deployment. As a non-noble-metal substitute, nickel and nickel alloy catalysts offer competitiveness but are typically limited to alkaline media due to corrosion in acidic environments.[11,12] In contrast, molybdenum sulfide (MoS_x) stands out for its excellent stability over a wide pH range [13,14], making it a promising HER catalyst for Sb_2Se_3 and other semiconductor materials such as Cu_2O and GaInP. [15–19] This catalyst can facilitate reactions in highly acidic conditions (pH 0–1) without protective overlayers such as TiO_2.[20,21]

Various preparation methods have been employed to maximize the density of the reactive sites of the MoS_x catalyst. One promising category of these MoS_x catalysts is molybdenum sulfide clusters, which, unlike the electrochemically inert basal planes observed in MoS_2, have maximized catalytic activity per molybdenum ion with an increased number of active sites for a given geometric surface area.[22] Furthermore, it has been observed that the efficiency of the photoabsorber is hindered by thicker layers of MoS_2. However, a thin layer of the molybdenum

clusters could fulfil the catalytic requirements, thereby removing any insulation effects from thicker catalyst layers.[14]

Herein, we report the suitability of versatile and easy-to-deposit catalysts directly on Sb_2Se_3, which include molybdenum sulfide clusters in different configurations, such as $[Mo_3S_4(H_2O)_9]Cl_4$ ($[Mo_3S_4]^{4+}$) and $(NH_4)_2[Mo_3S_{13}]\cdot 2H_2O$ ($[Mo_3S_{13}]^{2-}$). These earth-abundant catalysts can provide up to 20 mA cm^{-2} at –0.3 V versus reversible hydrogen electrode (RHE) with only a few nanometers thick layers, matching the photocurrents obtained with heterogenous co-catalysts such as platinum.[23] The easy deposition and simplicity of these molecular catalysts make them an excellent candidate for translation to other systems such as photocatalytic particles. The stability and loading of these catalysts have been studied using XPS and Raman.

The Sb_2Se_3 thin films in **Figure 1a** form the basis for most devices in this study. The films are soaked in either $[Mo_3S_4(H_2O)_9]Cl_4$ ($[Mo_3S_4]^{4+}$) or $(NH_4)_2[Mo_3S_{13}]\cdot 2$ H2O ($[Mo_3S_{13}]^{2-}$) solution for 12 hours to deposit the hydrogen evolution reaction (HER) catalyst. Finally, the films are annealed at 120°C to improve catalyst adhesion without altering molecular integrity. This was confirmed by Raman measurements which showed identical peaks before and after annealing. The $[Mo_3S_4]^{4+}$ illustrated in Figure 1b is synthesized from the reaction of ammonium tetrathiomolybdate with sodium borohydride and HCl in air.[24,25] Crystals suitable for single-crystal X-ray diffraction (XRD) were obtained after anion exchange with p-toluenesulfonic acid. The $[Mo_3S_{13}]^{2-}$ shown in Figure 1c was synthesized according to procedures developed by Streb and co-workers,[26] starting from ammonium heptamolybdate. A reaction with elemental sulphur and ammonium sulphide over four days yields the $[Mo_3S_{13}]^{2-}$ as dark red crystals suitable for X-ray crystallography. Mimicking the MoS_2 catalytically active edge sites, [27,28] molybdenum sulfide clusters have a maximum dimension of approximately 0.7 nm with a high ratio of active sites to

non-active ones (e.g., the basal plane in MoS_2); therefore, more active species and thus catalytically active sites can be packed on the photoabsorber surface, increasing reactivity with a thinly deposited catalyst layer ranging between 5–30 nm, as observed from the profilometer measurements reported in Table S1.

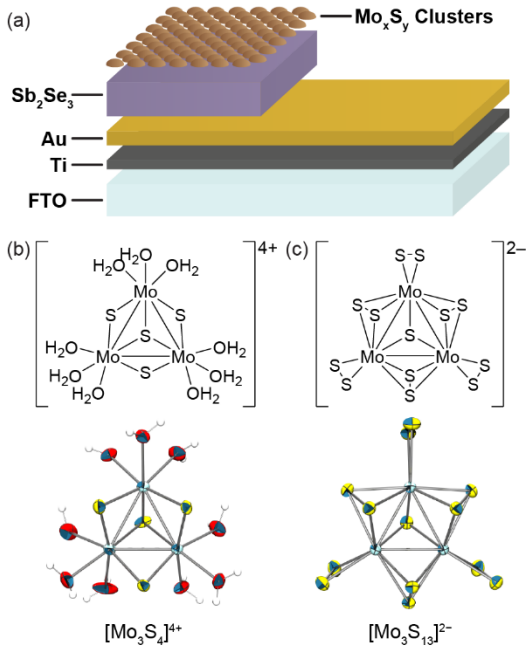

Figure 1 – (a) Typical stack of Sb_2Se_3 samples with a catalyst consisting of an FTO/Ti/Au/Sb_2Se_3/Mo_3S_x configuration. Molecular structure and ellipsoid displacement plots of (b) $[Mo_3S_4]^{4+}$ and (c) $[Mo_3S_{13}]^{2-}$. Ellipsoids represent a 50% probability. Counterions Cl_4^{4-} for (b), $(NH_4)_2^{2+}$ for (c) and solvent molecules are omitted for clarity.

Firstly, to investigate each catalyst's activity in the dark cyclic voltammetry (CV) cycled from 0.6 to –1.3 V versus RHE for 10 cycles in 1 M H_2SO_4 electrolyte (pH 0) was conducted for each sample. **Figure S1** displays the CV, revealing that $[Mo_3S_{13}]^{2-}$ exhibits a lower overpotential (approximately 300 mV less) compared to $[Mo_3S_4]^{4+}$ and maintains greater stability in 1 M H_2SO_4 electrolyte. Tafel plots of the two catalysts are given in Figure S1b. Typically, similar slopes among a family of catalysts in a Tafel plot imply a shared mechanism. However, the observed

Tafel slopes for the two molybdenum sulfur clusters, $[Mo_3S_{13}]^{2-}$ (62 mV/dec) and $[Mo_3S_4]^{4+}$ (107 mV/dec), are distinct and indicate different mechanisms for the catalytic reaction.

As observed in the literature, the concentration of the catalyst solution and, therefore, the catalyst loading influences the performance of the devices.[27] To find the optimum concentration of each catalyst, three different catalyst concentrations were tested. The concentration of the catalyst solution was optimized at 2 mM based on measurements observed in **Figure S2**. Devices at this concentration outperformed others, particularly between -0.3 and -0.1 V vs RHE in $[Mo_3S_4]^{4+}$ and between -0.2 and 0.0 V vs RHE in $[Mo_3S_{13}]^{2-}$. Meanwhile at 3 mM, increased dark current was observed for both catalysts in the range of -0.3 to -0.25 V vs RHE. While these results were reproducible, sample-to-sample variation could account for the slight differences observed. Subsequently, the $[Mo_3S_4]^{4+}$ and $[Mo_3S_{13}]^{2-}$ catalysts on top of the Sb_2Se_3 photoabsorber were measured in 1 M H_2SO_4 (pH 0) under 1 sun illumination, between 0.1 to –0.3 V versus RHE. As observed in **Figure 2a**, the $[Mo_3S_4]^{4+}$ and $[Mo_3S_{13}]^{2-}$ catalysts produced 16.0 mA cm^{-2} and 17.5 mA cm^{-2} at - 0.2 V versus RHE, respectively. With an onset potential of 0.05 V versus RHE, the $[Mo_3S_{13}]^{2-}$ has a better overall performance than the $[Mo_3S_4]^{4+}$ with a –0.02 V versus RHE onset. This difference is attributed to the different overpotentials of the two catalysts (see also Figure S1). This leads to a shift of the JV curve of the $[Mo_3S_4]^{4+}$ to more negative potentials, while the $[Mo_3S_{13}]^{2-}$ catalyst device exhibits a photocurrent of approximately 2.5 mA cm^{-2} higher at -0.2 V vs RHE compared to the $[Mo_3S_4]^{4+}$ catalyst device indicated by their J-V curves. Figure 2b illustrates that the $[Mo_3S_{13}]^{2-}$ catalyst has a higher incident photon to current conversion efficiency (IPCE) between 400–850 nm at a similar applied potential, indicating less surface recombination and more efficient charge collection compared to $[Mo_3S_4]^{4+}$, which suffers from slower charge transfer due to higher overpotential. Both catalysts have similar IPCE in the 850-1100 nm range,

as differences in extinction coefficients of Sb_2Se_3 affect photon absorption and charge carrier generation. In the 400-850 nm range, high charge density near the semiconductor-electrolyte interface enhances $[Mo_3S_{13}]^{2-}$ performance. In contrast, the 850-1100 nm range sees charge generation in the semiconductor bulk, resulting in similar IPCE for both. The higher overpotential for $[Mo_3S_4]^{4+}$ shown in Figure S1 underscores the $[Mo_3S_{13}]^{2-}$ catalyst's efficiency under conditions of high charge density at the electrolyte interface. The integrated currents in **Figure S3** are slightly higher than the values observed in the CV measurements above. The slight discrepancy in values can be attributed to the light intensity dependence of the Sb_2Se_3 devices, as shown in previous studies.[29] Furthermore, the activity of both catalysts was investigated across various pH levels. As shown in Figure S4, both catalysts exhibit a similar trend, performing best at pH 0, although they remain effective at more basic pH levels as well. This study highlights the flexibility and adaptability of these catalysts in diverse pH environments; however, stability remains limited on FTO.

As observed in **Figure 2c**, high faradaic efficiencies (FE) of up to 100% for the HER were obtained for both samples as quantified with gas chromatography. $[Mo_3S_{13}]^{2-}$ showed a FE of 103±7% (**Table S2**) after 10 minutes of 1 sun illumination at an applied potential of –0.2 V versus RHE. Under the same conditions, $[Mo_3S_4]^{4+}$ showed varying values with an average FE of 88±17% (**Table S3**). The larger error for the GC measurements with $[Mo_3S_4]^{4+}$ likely results from the lower photocurrent and, therefore, the longer time for the mass transport of hydrogen from the solution to the headspace, where it can be measured by GC.

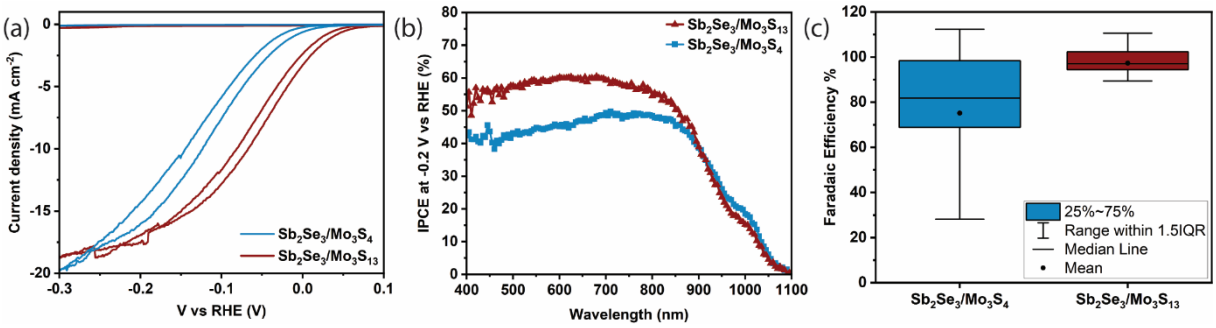

Figure 2 – (a) Cyclic voltammetry measurements versus RHE in 1 M H_2SO_4 under simulated 1 sun illumination (b) IPCE measurements in 1 M H_2SO_4 at –0.2 V versus RHE under 1% sun-white light bias (c) Faradaic efficiency of $[Mo_3S_4]^{4+}$ and $[Mo_3S_{13}]^{2-}$ measured at –0.2 V versus RHE under illumination by a white LED light (~ 1 sun).

The lower FE can also be attributed to the lower stability and faster degradation of the $[Mo_3S_4]^{4+}$ species. On the other hand, some of the $[Mo_3S_{13}]^{2-}$ samples were stable for over 1.5 hours under harsh working conditions with high FE. This can be observed in Table S4, where FE measurements at different times are presented. CV measurements of bare Sb_2Se_3 photocathode without catalysts (**Figure S5a**) were measured under illumination with light chopping which showed negligible dark currents and no photocurrent. $[Mo_3S_4]^{4+}$ catalyst, which is insoluble in pure H_2O (in contrast to $[Mo_3S_{13}]^{2-}$), was dissolved in 1 M HCl. To test the effects of the HCl solution, a bare Sb_2Se_3 was soaked in HCl which showed similar performance to the bare Sb_2Se_3 device (Figure S5a). The only observable difference is that the oxidation and reduction peaks seen in bare Sb_2Se_3 are considerably reduced in magnitude, implying that the HCl may have an etching property, removing oxides from the surface of the Sb_2Se_3 as previously studied.[29] As Pt is the benchmark catalyst for HER, a bare Sb_2Se_3 film was deposited with 2 nm of Pt and measured under illumination with light chopping. As shown in Figure S4b, the dark current observed with the Pt catalyst is considerably increased compared to that of the bare Sb_2Se_3 alone. However, no photocurrent is observed with

the Pt catalyst (the Pt catalyst is known to be most effective on the Sb_2Se_3 when combined with a TiO_2 overlayer, which was not investigated in this work). The stability of each molybdenum sulfide cluster as a catalyst was investigated by measuring them through 60 cycles of CV at 10 mV s^{-1} between 0.1 V to –0.3 V versus RHE, corresponding to 80 minutes of measurement time (**Figure S6**). The $[Mo_3S_{13}]^{2-}$ shows an improved onset and current in the first 5 cycles, then stabilizes for 20 cycles, and then starts to degrade slowly. Furthermore, chronoamperometric stability tests were conducted to evaluate the long-term stability of the catalysts (Figure S6c). The $[Mo_3S_{13}]^{2-}$ catalyst exhibits a characteristic stability curve similar to the CV sweeps. The initial improvement in the current can be attributed to an increase in activity resulting from the partial exchange of disulfide ligands with aqua ligands. This substitution affects the kinetics of the hydrogen evolution reaction, making it more favorable. However, a complete exchange of disulfides for aqua ligands can lead to decreased activity due to the loss of these hydrogen evolution active sites leading to very high free energies of the Volmer step. [30,31] In contrast, the $[Mo_3S_4]^{4+}$ catalyst shows only degradation with time, with the film (Au, Sb_2Se_3 and catalyst) peeling off after approximately two hours, rendering longer stability tests impossible. A partial peeling also occurs with the $[Mo_3S_{13}]^{2-}$ catalyst, contributing to the decrease in current, which could imply that the catalyst is not the limiting factor in such stability tests. This catastrophic failure is likely due to aggressive bubble formation penetrating beneath the film, which must be addressed and optimized for further long-term stability studies.

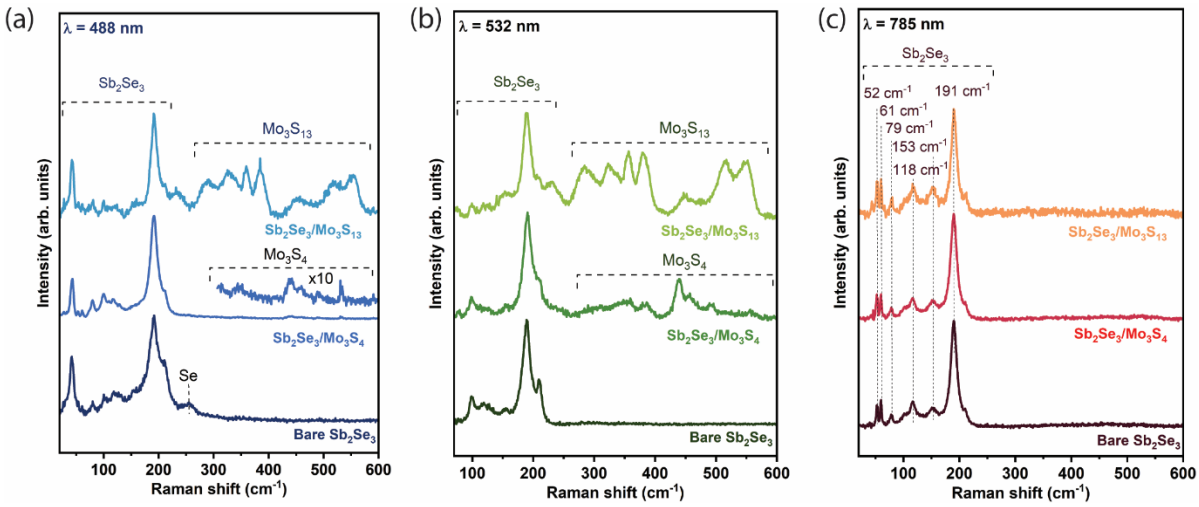

Figure 3 – (a) Raman spectra of a typical bare Sb_2Se_3 sample, Sb_2Se_3 + $[Mo_3S_4]^{4+}$ and Sb_2Se_3 + $[Mo_3S_{13}]^{2-}$ at the laser excitation wavelengths of (a) 488 nm (b) 532 nm, and (c) 785 nm.

To assess the potential morphological effects of molybdenum catalysts on the Sb_2Se_3 surface, scanning electron microscopy (SEM) images were obtained (**Figure S7**). Differences observed between bare Sb_2Se_3 and catalyst-treated samples were attributed to the etching treatment before catalyst soaking, consistent with prior studies.[29] SEM images after PEC measurements showed no noticeable differences in the morphology of the films. As different films were measured for each image, the differences in grain size can be attributed to sample-to-sample or even region-to-region variation. Atomic force microscopy (AFM) studies (**Figure S8**) further confirmed no discernible changes in the sample's surface morphology due to catalyst deposition. Ultraviolet-visible-near infrared diffuse reflectance spectroscopy (UV-Vis-NIR DRS) provided insights into the surface properties of samples pre and post catalyst deposition. **Figure S9a** shows similar reflectance spectra for bare Sb_2Se_3 and Sb_2Se_3 with $[Mo_3S_4]^{4+}$, while Figure S9b reveals increased reflectance in the blue region for $[Mo_3S_{13}]^{2-}$, corresponding to a faint brown color observed after $[Mo_3S_{13}]^{2-}$ deposition. Raman measurements with 488 nm, 532 nm and 785 nm excitation wavelengths were performed on bare Sb_2Se_3, Sb_2Se_3/$[Mo_3S_4]^{4+}$ clusters as a catalyst, and Sb_2Se_3/ $[Mo_3S_{13}]^{2-}$ (**Figure**

3). Raman measurements with 488 and 532 nm excitation wavelengths reveal clear patterns belonging to $[Mo_3S_4]^{4+}$ and $[Mo_3S_{13}]^{2-}$ phases, as shown in Figures 3a and 3b, respectively. This behavior is expected, as both 488 nm and 532 nm lasers have penetration depths corresponding to about 50 and 100 nm, respectively. This reduces the ratio of $Sb_2Se_3/[Mo_3S_4]^{4+}$, and $Sb_2Se_3/[Mo_3S_{13}]^{2-}$ probed volumes, rendering these laser excitations more sensitive to detecting clusters on the surface of Sb_2Se_3. In the spectra of Sb_2Se_3 with $[Mo_3S_4]^{4+}$ clusters, intense Raman peaks at 354, 440, 456 and 493 cm^{-1} are observed, which are not featured in the Raman spectra measured on the reference Sb_2Se_3 with both 488 nm and 532 nm excitations. These peak positions are in good agreement with the Raman peak positions of $[Mo_3S_4]^{4+}$ reported in the literature.[32] Furthermore, in the Raman spectra of Sb_2Se_3 with $[Mo_3S_{13}]^{2-}$ clusters, peaks at 285, 329, 360, 385, 453, 518 and 552 cm^{-1} in addition to peaks belonging to the Sb_2Se_3 phase were identified. These peaks are in good agreement with the Raman peak positions of $[Mo_3S_{13}]^{2-}$ phase reported in the literature.[33] The comparison of Raman spectra measured with 785 nm does not reveal any significant differences in the spectral features, including intensity, width and position of Raman peaks among the three samples. Only Raman peaks corresponding to the Sb_2Se_3 phase are observed at this wavelength, as shown in Figure 3c.[23] This indicates that the presence of $[Mo_3S_4]^{4+}$ and $[Mo_3S_{13}]^{2-}$ clusters on the surface of Sb_2Se_3 do not induce any structural changes in the Sb_2Se_3 layer. This was corroborated by XRD measurements (**Figure S10**), showing no changes in crystal orientation before and after catalyst depositions. Additionally, observation of the Raman peaks belonging to the $[Mo_3S_4]^{4+}$ and $[Mo_3S_{13}]^{2-}$ phases are not expected for this excitation wavelength, as the probed volume of Sb_2Se_3 material is about 50 times higher than the probed volume of either $[Mo_3S_4]^{4+}$ or $[Mo_3S_{13}]^{2-}$. Furthermore, the stability and integrity of the molecular catalysts were

confirmed by measuring Raman after PEC measurements. As observed in Figure S11, the fingerprint regions for both catalysts are still visible at 532 nm after PEC measurements.

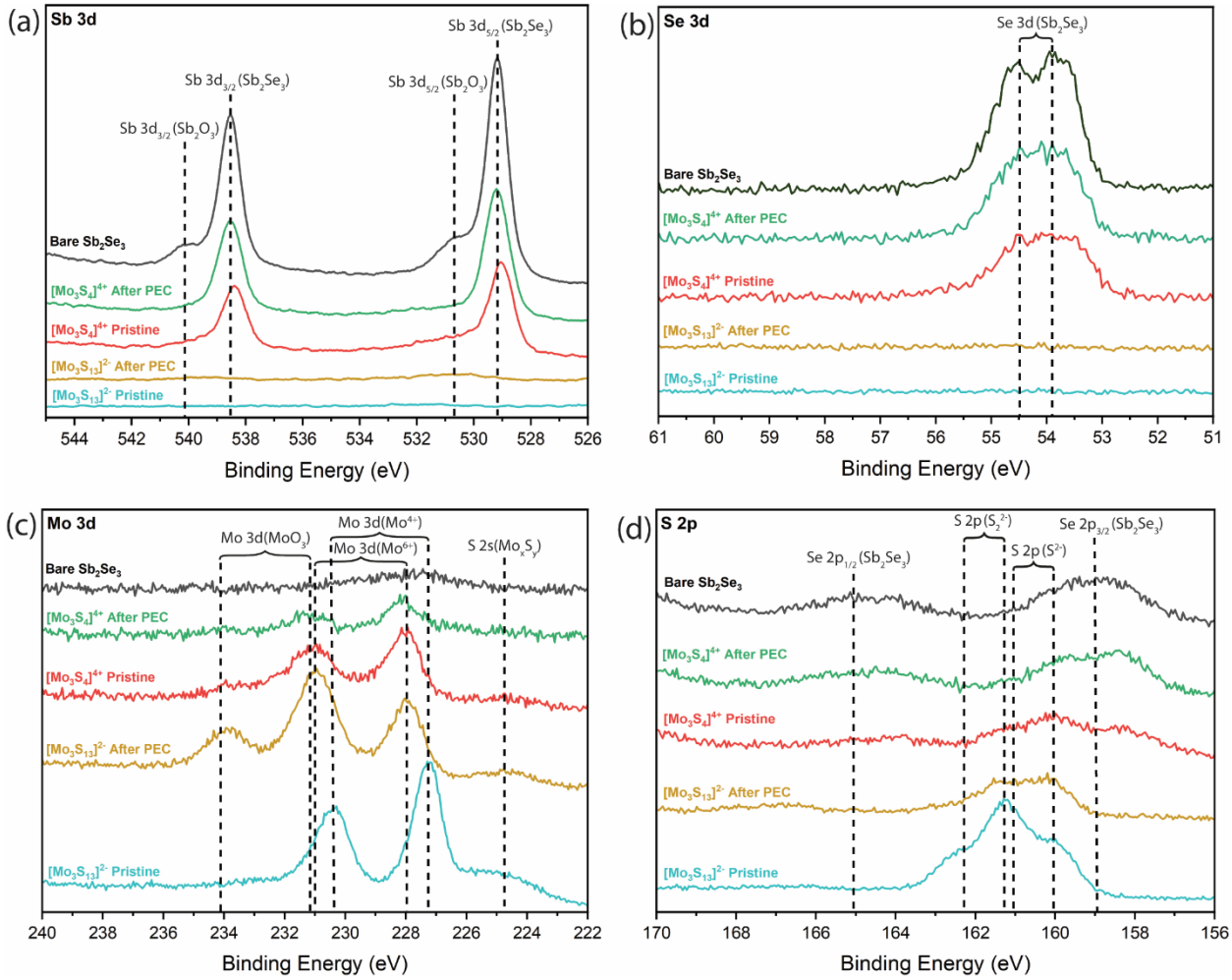

Figure 4 - XPS spectra (a) Sb 3d (b) Se 3d (c) Mo 3d and (d) S 2p for bare and catalysed samples measured before and after photoelectrocatalysis. Dashed reference lines are extracted from the NIST database.[34]

While the mechanism of action of molybdenum sulphide catalysts is still debated, there are currently two fundamentally different theories of how HER occurs on Mo_3S_x. One is a "molybdenum based" catalysis whilst the other is "sulphur based".[18] In the molybdenum-based

catalysis, unsaturated Mo sites (originating from the loss of terminal disulphides in $[Mo_3S_{13}]^{2-}$) serve as both a redox-active element and a site for substrate binding. In this system, molybdenum hydride is generated which is then protonated to liberate H_2.[32] Meanwhile, in the sulphur-based system, disulfides play the dual role of proton binder and redox-active component.[35] In both theories, a molecular system would mean that there are more active sites per unit area for H_2 evolution as the concentration of unsaturated Mo sites in both $[Mo_3S_4]^{4+}$ and $[Mo_3S_{13}]^{2-}$ and terminal disulphides in $[Mo_3S_{13}]^{2-}$ are higher compared to MoS_2 thin films. Based on the electrochemical and X-ray photoelectron spectroscopy (XPS) results in this study, it is hypothesised that both H_2 evolution mechanisms are in action in conjunction as there are no terminal disulphides in the $[Mo_3S_4]^{4+}$ clusters, however, the higher activity of $[Mo_3S_{13}]^{2-}$ is likely due to the contributions from the disulphide based hydrogen evolution leading to a better performance.[36] Figures 4a and 4b substantiate a conformal $[Mo_3S_{13}]^{2-}$ layer with at least 6 nm thickness (which is the approximate probing depth of the Se 3d line in this measurement). This is indicated by the absence of the Sb_2Se_3 substrate in both the Sb 3d and Se 3d spectra of both the pristine and post-PEC films. Conversely, the pristine $[Mo_3S_4]^{4+}$ layer is thinner (and/or not conformal) and appears to decrease further after PEC measurements, as evidenced by the visible Sb 3d and Se 3d signals. These findings suggest a homogeneous deposition of $[Mo_3S_{13}]^{2-}$ across the substrate, as the absence of a substrate emission implies uniform coverage. Figures 4c and 4d highlight distinctions between the two catalysts. The Mo 3d spectra indicate differing oxidation states for the $[Mo_3S_4]^{4+}$ and $[Mo_3S_{13}]^{2-}$ catalysts. The pristine $[Mo_3S_{13}]^{2-}$ catalyst shows the presence of molybdenum in Mo^{4+} form, whilst the post-PEC $[Mo_3S_{13}]^{2-}$ catalyst reveals a shift in molybdenum's core level, indicating an oxidation state of Mo^{6+}, accompanied by a MoO_3 peak. This implies the loss of some disulfides, exposing unsaturated Mo sites and enabling molybdenum-

based catalysis in conjunction with the sulphur-based catalysis. Meanwhile, the S 2p spectrum of $[Mo_3S_{13}]^{2-}$ initially shows a high concentration of disulfides (S_2^{2-}), which decreases slightly post-PEC measurements. Conversely, the Mo 3d signals for $[Mo_3S_4]^{4+}$ remain unchanged but decrease in intensity post-PEC measurements. The $[Mo_3S_4]^{4+}$ S 2p peaks only represent sulfide bonds (S^{2-}), diminishing in intensity post-PEC measurements. NAPXPS measurements in Figure S12, illustrate a similar trend but must be interpreted with caution due to the high signal-to-noise ratio. They indicate that more catalysts could be loaded on the surface of Sb_2Se_3 in the case of $[Mo_3S_{13}]^{2-}$ compared to $[Mo_3S_4]^{4+}$ during the same soaking time and concentration. This was based on the smaller Se 3s substrate peak and more prominent Mo and S peaks for $[Mo_3S_{13}]^{2-}$. The Se 3s substrate peak remained constant during exposure to water vapor, indicating stability. This effect was corroborated by **Figure S12c and d**, where Se 3d peaks were observed for $[Mo_3S_4]^{4+}$ but not for $[Mo_3S_{13}]^{2-}$. Furthermore, $[Mo_3S_{13}]^{2-}$ clusters initially displayed the expected stoichiometry, but this changed under operation, as evidenced in Figure S12b. The spectra indicated that the coverage of $[Mo_3S_{13}]^{2-}$ was initially very high, but after CV cycles, the Mo coverage dropped but did not entirely disappear. After CV measurements at different potentials, a chemical shift towards higher binding energy for Mo 3d was observed.

In summary, two molybdenum sulfide cluster species, $[Mo_3S_4]^{4+}$ and $[Mo_3S_{13}]^{2-}$, were thoroughly examined as co-catalysts on Sb_2Se_3 for photoelectrochemical hydrogen evolution. These clusters piqued interest due to their augmented active sites in comparison to MoS_2 which possesses a catalytically inert basal plane. Throughout this study, it was discovered that $[Mo_3S_{13}]^{2-}$ excelled as a catalyst when a thin layer was deposited on Sb_2Se_3. Remarkably, even a few tens of nanometers of catalyst deposited by soaking exhibited remarkable stability, observed via XPS after extended use. Paired with Sb_2Se_3, this catalyst achieved up to 100% faradaic efficiency and a

current density of 17.5 mA cm^{-2} at –0.2 V versus RHE. With additional refinement and the application of previously established treatments such as $AgNO_3$ treatment and sulfurization, this catalyst, when applied to Sb_2Se_3, can potentially demonstrate exceptional performance and improved stability.

Notes

The authors declare no competing financial interest

This work was supported by the University of Zurich, URPP LightChEC, and SNF Project # 184737. J.B. acknowledges funding from the University of Zurich (UZH Candoc Grant, grant no. [FK-23-093]). J.T.D. acknowledges funding from the European Union's Horizon 2020 under MCSA Grant No. 801459, FP-RESOMUS.

(1) *Climate Change 2022: Impacts, Adaptation and Vulnerability | Climate Change 2022: Impacts, Adaptation and Vulnerability*. https://www.ipcc.ch/report/ar6/wg2/ (accessed 2023-09-19).

(2) Odenweller, A.; Ueckerdt, F.; Nemet, G. F.; Jensterle, M.; Luderer, G. Probabilistic Feasibility Space of Scaling up Green Hydrogen Supply. *Nat Energy* **2022**, *7* (9), 854–865. https://doi.org/10.1038/s41560-022-01097-4.

(3) Schneidewind, J. How Much Technological Progress Is Needed to Make Solar Hydrogen Cost-Competitive? *Adv Energy Mater* **2022**, *12* (18), 2200342. https://doi.org/10.1002/aenm.202200342.

(4) Zhang, X.; Schwarze, M.; Schomäcker, R.; van de Krol, R.; Abdi, F. F. Life Cycle Net Energy Assessment of Sustainable H2 Production and Hydrogenation of Chemicals in a Coupled Photoelectrochemical Device. *Nat Commun* **2023**, *14* (1), 991. https://doi.org/10.1038/s41467-023-36574-1.

(5) Yang, W.; Kim, J. H.; Hutter, O. S.; Phillips, L. J.; Tan, J.; Park, J.; Lee, H.; Major, J. D.; Lee, J. S.; Moon, J. Benchmark Performance of Low-Cost Sb2Se3 Photocathodes for Unassisted Solar Overall Water Splitting. *Nat Commun* **2020**, *11* (1), 861. https://doi.org/10.1038/s41467-020-14704-3.

(6) Chen, S.; Liu, T.; Zheng, Z.; Ishaq, M.; Liang, G.; Fan, P.; Chen, T.; Tang, J. Recent Progress and Perspectives on Sb2Se3-Based Photocathodes for Solar Hydrogen Production via Photoelectrochemical Water Splitting. *Journal of Energy Chemistry*. Elsevier April 1, 2022, pp 508–523. https://doi.org/10.1016/j.jechem.2021.08.062.

(7) Wijesinghe, U.; Longo, G.; Hutter, O. S. Defect Engineering in Antimony Selenide Thin Film Solar Cells. *Energy Advances*. Royal Society of Chemistry January 19, 2022, pp 12–33. https://doi.org/10.1039/d2ya00232a.

(8) Li, Z.; Liang, X.; Li, G.; Liu, H.; Zhang, H.; Guo, J.; Chen, J.; Shen, K.; San, X.; Yu, W.; Schropp, R. E. I.; Mai, Y. 9.2%-Efficient Core-Shell Structured Antimony Selenide Nanorod Array Solar Cells. *Nat Commun* **2019**, *10* (1), 125. https://doi.org/10.1038/s41467-018-07903-6.

(9) Luo, Y.; Chen, G.; Chen, S.; Ahmad, N.; Azam, M.; Zheng, Z.; Su, Z.; Cathelinaud, M.; Ma, H.; Chen, Z.; Fan, P.; Zhang, X.; Liang, G. Carrier Transport Enhancement Mechanism in Highly Efficient Antimony Selenide Thin-Film Solar Cell. *Adv Funct Mater* **2023**, *33* (14), 2213941. https://doi.org/10.1002/adfm.202213941.

(10) de Araújo, M. A.; Costa, M. B.; Mascaro, L. H. Improved Photoelectrochemical Hydrogen Gas Generation on Sb 2 S 3 Films Modified with an Earth-Abundant MoS x Co-Catalyst. *ACS Appl Energy Mater* **2022**, *5* (1), 1010–1022. https://doi.org/10.1021/acsaem.1c03374.

(11) Huo, L.; Jin, C.; Jiang, K.; Bao, Q.; Hu, Z.; Chu, J. Applications of Nickel-Based Electrocatalysts for Hydrogen Evolution Reaction. *Advanced Energy and Sustainability*

Research. John Wiley & Sons, Ltd April 26, 2022, p 2100189. https://doi.org/10.1002/aesr.202100189.

(12) Liu, X.; Ni, K.; Wen, B.; Guo, R.; Niu, C.; Meng, J.; Li, Q.; Wu, P.; Zhu, Y.; Wu, X.; Mai, L. Deep Reconstruction of Nickel-Based Precatalysts for Water Oxidation Catalysis. *ACS Energy Lett* **2019**, *4* (11), 2585–2592. https://doi.org/10.1021/acsenergylett.9b01922.

(13) Zheng, H.-L.; Zhao, J.-Q.; Zhang, J.; Lin, Q. Acid–Base Resistant Ligand-Modified Molybdenum–Sulfur Clusters with Enhanced Photocatalytic Activity towards Hydrogen Evolution. *J Mater Chem A Mater* **2022**, *10* (13), 7138–7145. https://doi.org/10.1039/D2TA00352J.

(14) Costa, M. B.; Lucas, F. W. S.; Medina, M.; Mascaro, L. H. All-Electrochemically Grown Sb $_2$ Se $_3$ /a-MoS $_x$ Photocathodes for Hydrogen Production: The Effect of the MoS $_x$ Layer on the Surface Recombination and Photocorrosion of Sb $_2$ Se <sub>3<. *ACS Appl Energy Mater* **2020**, *3* (10), 9799–9808. https://doi.org/10.1021/acsaem.0c01413.

(15) Ding, Q.; Song, B.; Xu, P.; Jin, S. Efficient Electrocatalytic and Photoelectrochemical Hydrogen Generation Using MoS2 and Related Compounds. *Chem* **2016**, *1* (5), 699–726. https://doi.org/10.1016/j.chempr.2016.10.007.

(16) Britto, R. J.; Young, J. L.; Yang, Y.; Steiner, M. A.; LaFehr, D. T.; Friedman, D. J.; Beard, M.; Deutsch, T. G.; Jaramillo, T. F. Interfacial Engineering of Gallium Indium Phosphide Photoelectrodes for Hydrogen Evolution with Precious Metal and Non-Precious Metal Based Catalysts. *J Mater Chem A Mater* **2019**, *7* (28), 16821–16832. https://doi.org/10.1039/c9ta05247j.

(17) Morales-Guio, C. G.; Tilley, S. D.; Vrubel, H.; Grätzel, M.; Hu, X. Hydrogen Evolution from a Copper(I) Oxide Photocathode Coated with an Amorphous Molybdenum Sulphide Catalyst. *Nat Commun* **2014**, *5* (1), 3059. https://doi.org/10.1038/ncomms4059.

(18) Grutza, M.-L.; Rajagopal, A.; Streb, C.; Kurz, P. Hydrogen Evolution Catalysis by Molybdenum Sulfides (MoSx): Are Thiomolybdate Clusters like [Mo3S13]2- Suitable Active Site Models? *Sustain Energy Fuels* **2018**, *2* (9), 1893–1904. https://doi.org/10.1039/c8se00155c.

(19) Laursen, A. B.; Kegnæs, S.; Dahl, S.; Chorkendorff, I. Molybdenum Sulfides - Efficient and Viable Materials for Electro - And Photoelectrocatalytic Hydrogen Evolution. *Energy and Environmental Science*. The Royal Society of Chemistry January 25, 2012, p 5577. https://doi.org/10.1039/c2ee02618j.

(20) Prabhakar, R. R.; Septina, W.; Siol, S.; Moehl, T.; Wick-Joliat, R.; Tilley, S. D. Photocorrosion-Resistant Sb2Se3 Photocathodes with Earth Abundant MoS: X Hydrogen Evolution Catalyst. *J Mater Chem A Mater* **2017**, *5* (44), 23139–23145. https://doi.org/10.1039/c7ta08993g.

(21) Gu, J.; Aguiar, J. A.; Ferrere, S.; Steirer, K. X.; Yan, Y.; Xiao, C.; Young, J. L.; Al-Jassim, M.; Neale, N. R.; Turner, J. A. A Graded Catalytic-Protective Layer for an Efficient and

Stable Water-Splitting Photocathode. *Nat Energy* **2017**, *2* (2), 16192. https://doi.org/10.1038/nenergy.2016.192.

(22) Batool, S.; Nandan, S. P.; Myakala, S. N.; Rajagopal, A.; Schubert, J. S.; Ayala, P.; Naghdi, S.; Saito, H.; Bernardi, J.; Streb, C.; Cherevan, A.; Eder, D. Surface Anchoring and Active Sites of $[Mo_3S_{13}]^{2-}$ Clusters as Co-Catalysts for Photocatalytic Hydrogen Evolution. *ACS Catal* **2022**, *12* (11), 6641–6650. https://doi.org/10.1021/acscatal.2c00972.

(23) Adams, P.; Schnyder, R.; Moehl, T.; Bühler, J.; Alvarez, A. L.; Dimitrievska, M.; McKenna, K.; Yang, W.; Tilley, S. D. Post-Synthetic Silver Ion and Sulfurization Treatment for Enhanced Performance in Sb 2 Se 3 Water Splitting Photocathodes. *Adv Funct Mater* **2023**, 2310596. https://doi.org/10.1002/adfm.202310596.

(24) Shibahara, T.; Yamasaki, M.; Sakane, G.; Minami, K.; Yabuki, T.; Ichimura, A. Syntheses and Electrochemistry of Incomplete Cubane-Type Clusters with M3S4 Cores (M = Molybdenum, Tungsten). X-Ray Structures of [W3S4(H2O)9](CH3C6H4SO3)4.Cntdot.9H2O, Na2[W3S4(Hnta)3].Cntdot.5H2O, and (BpyH)5[W3S4(NCS)9].Cntdot.3H2O. *Inorg Chem* **1992**, *31* (4), 640–647. https://doi.org/10.1021/ic00030a022.

(25) Dimitri Coucouvanis. *Inorganic Syntheses*; Coucouvanis, D., Ed.; Inorganic Syntheses; Wiley, 2002; Vol. 33. https://doi.org/10.1002/0471224502.

(26) Dave, M.; Rajagopal, A.; Damm-Ruttensperger, M.; Schwarz, B.; Nägele, F.; Daccache, L.; Fantauzzi, D.; Jacob, T.; Streb, C. Understanding Homogeneous Hydrogen Evolution Reactivity and Deactivation Pathways of Molecular Molybdenum Sulfide Catalysts. *Sustain Energy Fuels* **2018**, *2* (5), 1020–1026. https://doi.org/10.1039/c7se00599g.

(27) Kibsgaard, J.; Jaramillo, T. F.; Besenbacher, F. Building an Appropriate Active-Site Motif into a Hydrogen-Evolution Catalyst with Thiomolybdate [Mo3S13]2- Clusters. *Nat Chem* **2014**, *6* (3), 248–253. https://doi.org/10.1038/nchem.1853.

(28) Huang, Z.; Luo, W.; Ma, L.; Yu, M.; Ren, X.; He, M.; Polen, S.; Click, K.; Garrett, B.; Lu, J.; Amine, K.; Hadad, C.; Chen, W.; Asthagiri, A.; Wu, Y. Dimeric [Mo2S12]2- Cluster: A Molecular Analogue of MoS2 Edges for Superior Hydrogen-Evolution Electrocatalysis. *Angewandte Chemie - International Edition* **2015**, *54* (50), 15181–15185. https://doi.org/10.1002/anie.201507529.

(29) Adams, P.; Creazzo, F.; Moehl, T.; Crockett, R.; Zeng, P.; Novotny, Z.; Luber, S.; Yang, W.; Tilley, S. D. Solution Phase Treatments of Sb 2 Se 3 Heterojunction Photocathodes for Improved Water Splitting Performance. *J Mater Chem A Mater* **2023**, *11* (15), 8277–8284. https://doi.org/10.1039/D3TA00554B.

(30) Dave, M.; Rajagopal, A.; Damm-Ruttensperger, M.; Schwarz, B.; Nägele, F.; Daccache, L.; Fantauzzi, D.; Jacob, T.; Streb, C. Understanding Homogeneous Hydrogen Evolution Reactivity and Deactivation Pathways of Molecular Molybdenum Sulfide Catalysts. *Sustain Energy Fuels* **2018**, *2* (5), 1020–1026. https://doi.org/10.1039/C7SE00599G.

(31) Escalera-López, D.; Iffelsberger, C.; Zlatar, M.; Novčić, K.; Maselj, N.; Van Pham, C.; Jovanovič, P.; Hodnik, N.; Thiele, S.; Pumera, M.; Cherevko, S. Allotrope-Dependent Activity-Stability Relationships of Molybdenum Sulfide Hydrogen Evolution Electrocatalysts. *Nature Communications 2024 15:1* **2024**, *15* (1), 1–13. https://doi.org/10.1038/s41467-024-47524-w.

(32) Tran, P. D.; Tran, T. V.; Orio, M.; Torelli, S.; Truong, Q. D.; Nayuki, K.; Sasaki, Y.; Chiam, S. Y.; Yi, R.; Honma, I.; Barber, J.; Artero, V. Coordination Polymer Structure and Revisited Hydrogen Evolution Catalytic Mechanism for Amorphous Molybdenum Sulfide. *Nat Mater* **2016**, *15* (6), 640–646. https://doi.org/10.1038/nmat4588.

(33) Yuan, M.; Yao, H.; Xie, L.; Liu, X.; Wang, H.; Islam, S. M.; Shi, K.; Yu, Z.; Sun, G.; Li, H.; Ma, S.; Kanatzidis, M. G. Polypyrrole–Mo_3S_{13} : An Efficient Sorbent for the Capture of Hg^{2+} and Highly Selective Extraction of Ag^{+} over Cu^{2+}. *J Am Chem Soc* **2020**, *142* (3), 1574–1583. https://doi.org/10.1021/jacs.9b12196.

(34) *NIST X-ray Photoelectron Spectroscopy Database*. https://srdata.nist.gov/xps/ (accessed 2024-05-30).

(35) Lassalle-Kaiser, B.; Merki, D.; Vrubel, H.; Gul, S.; Yachandra, V. K.; Hu, X.; Yano, J. Evidence from in Situ X-Ray Absorption Spectroscopy for the Involvement of Terminal Disulfide in the Reduction of Protons by an Amorphous Molybdenum Sulfide Electrocatalyst. *J Am Chem Soc* **2015**, *137* (1), 314–321. https://doi.org/10.1021/JA510328M/SUPPL_FILE/JA510328M_SI_001.PDF.

(36) Batool, S.; Langer, M.; Myakala, S. N.; Heiland, M.; Eder, D.; Streb, C.; Cherevan, A. Thiomolybdate Clusters: From Homogeneous Catalysis to Heterogenization and Active Sites. *Advanced Materials* **2024**, *36* (7), 2305730. https://doi.org/10.1002/ADMA.202305730.

Supporting Information:

Molybdenum Sulfide Clusters as a Molecular Co-Catalyst on Antimony Selenide Photocathodes for Photoelectrochemical Hydrogen Evolution

Pardis Adams[†], Jan Bühler[†], Iva Walz[†], Thomas Moehl[†], Helena Roithmeyer[†],Olivier Blacque[†], Nicolò Comini[‡§], J. Trey Diulus[‡§], Roger Alberto[†], Sebastian Siol[‖], Mirjana Dimitrievska[‖], Zbynek Novotny[‡§], and S. David Tilley[†]**

[†] Department of Chemistry, University of Zurich, Winterthurerstrasse 190, Zurich, 8057, Switzerland

[‡] Department of Physics, University of Zurich, Winterthurerstrasse 190, Zurich, 8057, Switzerland

[§] Swiss Light Source, Paul Scherrer Institute, Villigen-PSI, Switzerland

[‖] Surface Science and Coating Technologies Lab/ Transport at Nanoscale Interfaces Lab, Swiss Federal Laboratories for Materials Science and Technology (EMPA), Ueberlandstrasse 129, Dübendorf, 8600, Switzerland

Corresponding Author

S. David Tilley – Department of Chemistry, University of Zurich, Winterthurerstrasse 190, Zurich, 8057, Switzerland, E-mail: david.tilley@chem.uzh.ch

Zbynek Novotny – Department of Physics, University of Zurich, Winterthurerstrasse 190, Zurich, 8057, Switzerland, E-mail: zbynek.novotny@pnnl.gov

Experimental Methods

General Information

Unless otherwise stated, all chemicals were of reagent grade or higher, obtained from commercial sources and used without further purification. Solvents for reactions were of p.a. grade; H_2O was ultrapure from a Milli-Q® Direct 8 water purification system. Deuterated solvents were purchased from Sigma Aldrich.

Catalyst Synthesis

$[Mo_3S_4(H_2O)_9]Cl_4$

Prepared according to a published procedure.[1,2]

Caution: Toxic H_2S is produced during the reaction. It is recommended to use gas washing bottles containing bleach.

To a solution of $(NH_4)_2[MoS_4]$ (1.00 g, 3.84 mmol) in H_2O (35 mL) were alternatingly added (1 mL each addition) aqueous HCl (6 M, 15 mL) and aqueous $NaBH_4$ (2 M, 15 mL). The brown reaction mixture was heated to 90 °C while air was passed through a glass syringe. After 22 h, a colour change to dark green was observed, and the mixture was cooled with an ice bath. Filtration and washing of the filter cake with aqueous HCl (1 M, 10 mL) afforded a green filtrate condensed in vacuo to roughly 5 mL. The crude product was purified over a Sephadex G-10 (10 g, bloomed in 1 M HCl, 1 M HCl as eluent) column. A green band of $[Mo_3S_3O]^{4+}$ (λ_{max} 605 nm) was eluted first before a band containing the dark green product (λ_{max} 620 nm). The product-containing fractions were diluted with H_2O (five times the original volume) and purified over a DOWEX

50WX2 (15 g, washed with 2 M HCl, 2 M as eluent) column. A light brown band of $[Mo_2O_2S_2]^{2+}$ was eluted first before a band of the dark green product. The solvent was evaporated in vacuo to afford $[Mo_3S_4(H_2O)_9]Cl_4$ (362 mg, 1.281 mmol, 39%) as a dark green powder.

FT-IR (KBr, cm^{-1}): 3390 (br, s), 3225 (s), 1622 (m), 1404 (m), 1195 (w), 960 (w), 847 (m), 806 (m), 570 (w), 493 (w).

HRMS (ESI) m/z calcd for $C_2H_6ClMo_3O_2S_4$ $[M-9\ H_2O+2\ OMe+Cl]^+$: 518.60958; found: 518.60871.

UV-Vis (1 M HCl, nm ($mol^{-1}\ dm^3\ cm^{-1}$)): λmax (ε)= 255 (7'945), 371 (3'475), 620 (172).

$(NH_4)_2[Mo_3S_{13}]\cdot 2\ H_2O$

Prepared according to a published procedure.[3]

$(NH_4)_2S_x$ (25 wt-%) solution was prepared by dissolving elemental sulphur (3.00 g) in $(NH_4)_2S$ (48 wt-%, 20 mL) and H_2O (20 mL). $(NH_4)_2[Mo_7O_{24}]\cdot 4\ H_2O$ (1.02 g, 0.825 mmol) was dissolved in H_2O (5 mL), and aqueous $(NH_4)_2S_x$ solution (25 wt-%, 30 mL) was added. The flask was covered with a watch glass, and the reaction mixture was heated to 95 °C for 96 h without stirring. Dark red crystals were formed together with solid elemental sulphur. The solids were collected by filtration, and the filter cake was washed with H_2O (3×10 mL), EtOH (3×10 mL), CS_2 (3×10 mL, until sulfur has fully dissolved) and Et_2O (3×10 mL). The filter cake was air dried to yield $(NH_4)_2[Mo_3S_{13}]\cdot 2\ H_2O$ (1.32 g, 1.70 mmol, 88%) as dark red crystals.

FT-IR (KBr, cm^{-1}): 3437 (br, m), 3081 (m), 2926 (m), 2781 (m), 1633 (w), 1566 (w), 1399 (s), 1385 (s), 544 (s), 506 (s), 459 (w).

HRMS (ESI) m/z calcd for $H_3Mo_3S_{13}$ $[M+3\ H]^+$: 712.37607; found: 712.37391.

UV-Vis (MeOH, nm (mol^{-1} dm^3 cm^{-1})): λmax (ε)= 267 (38'978), 425 (4'432).

Catalyst Characterization

FT-IR spectra were recorded on a SpectrumTwo FT-IR Spectrometer (Perkin–Elmer); samples were applied as KBr pellets. **High-resolution electrospray mass spectra (HR-ESI-MS)** were recorded on a timsTOF Pro TIMS-QTOF-MS instrument (Bruker Daltonics GmbH, Bremen, Germany). The samples were dissolved in MeOH at a ca. 50 µg mL^{-1} concentration and analyzed via continuous flow injection (2 µL min^{-1}). The mass spectrometer was operated in the positive or negative electrospray ionization mode at 4'000 V (-4'000 V) capillary voltage and −500 V (500 V) endplate offset with an N_2 nebulizer pressure of 0.4 bar and a dry gas flow of 4 L min^{-1} at 180 °C. Mass spectra were acquired in a mass range from m/z 50 to 2'000 at ca. 20'000 resolution (m/z 622) and at 1.0 Hz rate. The mass analyzer was calibrated between m/z 118 and 2'721 using an Agilent ESI-L low-concentration tuning mix solution (Agilent, USA) at a resolution of 20,000, giving a mass accuracy below 2 ppm. All solvents used were purchased in the best LC-MS quality. **UV-Vis** spectra were recorded on a Shimadzu UV-3600 Plus spectrophotometer.

PEC Device Synthesis

Pilkington's FTO TEC 15 substrates were first cut into 1×2.5 cm^2 pieces and then meticulously cleaned using a series of solvents: soapy distilled water, distilled water, acetone, and isopropyl alcohol (IPA). Following this cleaning process, they were dried with a nitrogen gun. Subsequently, the substrates underwent a 30 minute UV/ozone cleaning to eliminate surface contaminants. Next, a Safematic CCU-010 sputter coater was employed to apply a 10 nm thick layer of titanium (Ti) (acting as an adhesion layer) followed by a 150 nm thick layer of gold (Au) onto the FTO substrates (serving as a hole-extracting electrode, creating an ohmic contact with the photoabsorber). A three-electrode setup was utilized to carry out the electrodeposition of antimony (Sb) metal onto the FTO/Ti/Au substrates. The Sb electrodeposition solution consisted of 15 mM potassium antimony tartrate and 50 mM tartaric acid, with the pH adjusted to 1.3. An electrode potential of −0.3 V versus Ag/AgCl was applied to control the Sb thickness by monitoring the charge passed, limited to 1.4 C cm^{-2}. Careful attention was given to ensure uniform thickness and optimal performance during deposition. Subsequently, the resulting Sb substrates underwent a selenization process using a two-zone furnace. Selenium pellets were positioned around the substrate, and the chamber was purged with argon. The temperature was gradually increased to 350 °C at a rate of 15 °C per minute and held for 40 minutes. For the reference, Sb_2Se_3/Pt samples, a 2 nm thick platinum (Pt) layer was sputtered onto the photocathode. This method creates high-quality compact thin films without requiring advanced high vacuum equipment. However, it is crucial to exercise caution to prevent minor gas leaks that could lead to forming an Sb_2O_3 layer on top of the Sb_2Se_3.

Photoelectrochemical (PEC) Characterization of Sb_2Se_3

The photoelectrochemical performance of the photocathodes was evaluated using a BioLogic SP-200 potentiostat. This assessment followed a three-electrode setup, with simulated AM 1.5G illumination provided and calibrated to 100 mW cm^{-2} (1 sun) using a silicon diode sourced from PV Measurements, Inc. The electrolyte used was a 1 M H_2SO_4 solution with a pH of 0. The three-electrode configuration consisted of an Ag/AgCl reference electrode immersed in a 3 M KCl solution, a counter electrode made of freshly cleaned Pt wire, and the photocathode serving as the working electrode. Cyclic voltammetry (CV) measurements were conducted at a scan speed of 10 mV s^{-1}. The scans were performed by sweeping from positive to negative potential and then back to positive potential. The exact onset potential value was defined by extrapolating to zero current from the oxidative sweep at the HER peak. To define the photocathode area, epoxy (specifically Loctite 9461) was applied around an O-ring with an inner diameter of 7 mm and placed on the sample's surface. For measurements of incident photon-to-current efficiency (IPCE), a custom-built IPCE system was utilized. This system included a halogen light source, a double monochromator, and white light bias generated by an LED. IPCE measurements were also conducted within the aforementioned three-electrode configuration, maintaining a potential of –0.2 V versus RHE (Reversible Hydrogen Electrode). These measurements were performed with 5 nm wavelength intervals and a 1% white light bias.

Solution Treatments and Catalyst Deposition

In this section, all procedures were carried out following the synthesis of Sb_2Se_3 and preceding the catalyst soaking. Prior to any of these treatments, a layer of Teflon tape was applied to mask the

exposed Au surface. Subsequently, the Sb_2Se_3 thin films were briefly immersed in a transparent yellow solution of $(NH_4)_2S$ (10 wt%) for 5 seconds. They were then rinsed with distilled water and dried under a nitrogen stream (N_2). This particular sequence of steps was undertaken as the initial measure before further treatments, owing to its effectiveness in enhancing device performance, as previously detailed in our earlier publication.[4] For a 1 mM $[Mo_3S_4]^{4+}$ catalyst deposition, 7.20 mg of $[Mo_3S_4(H_2O)_9]Cl_4$ were dissolved in 10 ml 1 M HCl and sonicated for 30 minutes. Similarly, for 1 mM $[Mo_3S_{13}]^{2-}$ catalyst deposition, 7.77 mg $(NH_4)_2[Mo_3S_{13}]\cdot 2\ H_2O$ were dissolved in 10 ml distilled H_2O and sonicated for 30 minutes. Samples were placed in the catalyst solution and soaked for 12 hours at room temperature. They were then rinsed from the back and annealed at 120˚ C for 30 minutes. The same procedure was performed for the catalyst deposition on FTO.

Tafel Plot Analysis

The LSV measurements were conducted using an Ag/AgCl reference electrode in 1 M H_2SO_4, with a Pt counter electrode placed behind a frit to prevent oxygen entry, but still in the same electrolyte solution. The potential range applied was from 0.2 to –0.55 V vs RHE (against RHE) for $[Mo_3S_4]^{4+}$, and from 0.2 to -0.35 V vs RHE for $[Mo_3S_{13}]^{2-}$, with a scan rate of 0.5 mV/s. To stabilize the redox potential in the solution, hydrogen was bubbled electrochemically using two Pt wires connected to a second potentiostat. The Pt electrode generating oxygen was also behind a frit but remained in the same electrolyte solution. For the Tafel plot analysis, the applied potential was IR drop corrected using the formula: IR drop corrected potential = applied voltage – voltage drop, where the voltage drop was calculated by multiplying the current by the series resistance. The series resistance (30 ohms) was determined through electrochemical impedance spectroscopy

at 0.2 V. A linear fit was performed for both the initial rise in current (first redox event) and the subsequent redox event leading to H_2 generation. The latter fit was in the range of 0.1 to 1 mA/cm².

GC and Faradaic Efficiency

The produced hydrogen was measured on an Inficon Fusion Micro gas chromatograph with a molecular sieve column (5Å) and a μTCD. Argon was used as the carrier gas. Before starting the measurements, the samples were placed in a one-component cell with a reference and a counter electrode. They were degassed for 30 to 40 minutes with argon, and three baseline measurements were done before each sample measurement. The operation pressure was between 1.020 and 1.030 bar and kept constant with a pressure control system. The calibration (and associated calculations) are seen and described in the supplementary information, **Figure S10** and **Table S3**.

Morphology and Crystal Characterization

Top-view scanning electron microscopy (SEM) images of the Sb_2Se_3 thin films with and without different catalysts were acquired using a Zeiss Gemini 450 SEM. X-ray diffraction (XRD) analysis utilized the Rigaku Smartlab diffractometer. Reference cards for Sb_2Se_3 and Au were obtained from the Cambridge Crystallographic Data Centre (CCDC) database. The UV-3600 Plus instrument from Shimadzu, equipped with an integrating sphere, was employed for conducting diffuse reflectance measurements (DRS). An Asylum Research AFM (MFP-3D) was used to measure the work function of the samples. The probe used for the measurement was an AC240TM-R3. For calibration of the work function of the tip, a highly ordered pyrolytic graphite (HOPG)

was used, with a reported work function of ~4.6 eV.[5] To achieve a fresh HOPG surface, a piece of scotch tape was used to pull off a few top layers of the graphite, exposing a fresh, clean surface for calibration. The HOPG used was purchased from MikroMasch (Grade: ZYA). The open-source Gwyddion software package and the Asylum Research built-in software were used to analyse the AFM pictures further. The thickness of the samples was measured using the DektakXT Bruker stylus profilometer.

Raman

Raman measurements were acquired on a WITec Alpha 300 R confocal Raman microscope in backscattering geometry. Multiwavelength excitation Raman measurements using 488, 532 and 785 nm lasers were performed on all samples. The beam was focused on the sample with a microscope objective, resulting in a diameter spot of 800 nm for 488 nm laser, 1 μm for 532 nm laser, and 1.2 μm for 785 nm laser, and reaching a radiant power of the order of 300 μW. Laser power conditions were selected based on a power study, which involved measuring Raman spectrum at the same point on the material with increasing laser power densities, starting from the lowest power available. For each laser power, the spectrum was monitored for changes in peak positions, peak widths, or the appearance of new peaks. The highest power for which no changes in these parameters were observed was taken as the optimal laser power for measurements. The backscattered light was analyzed with two spectrometers: a 300 mm lens-based spectrometer with a grating of 1800 g/mm equipped with a thermoelectrically cooled CCD for 488 and 532 nm excitation and a 400 mm lens-based spectrometer with a grating of 1200 g/mm equipped with a

cooled deep-depletion CCD for 785 nm excitation. All spectra were calibrated based on the reference Si Raman spectrum.

XPS

All XPS spectra were recorded using the endstation described in the referenced literature.[6] XPS spectra were recorded using focused, linearly polarized light 4000 eV at the Phoenix I beamline at the Swiss Light Source, with a probing depth of approximately 30 nm in liquid water. Spectra were recorded in high vacuum (HV) and at equilibrium electrolyte at a water vapor pressure of 25 mbar. Measurements were taken at three different potentials, which varied for each catalyst. P1(before onset potential), P2 (at onset potential) and P3 (after onset potential) were set to +0.22, +0.02 and –0.18 mV vs RHE for $[Mo_3S_4]^{+4}$, respectively. Moreover, P1, P2 and P3 were set to +0.05, –0.15 and –0.3 mV vs RHE for $[Mo_3S_{13}]^{2-}$, respectively. Peak fitting was performed in CasaXPS, and spectra were plotted in Origin Pro. The combined Mo 3d and S 2s region was fitted with two pairs of peaks for both Mo 3d and S2s. Two different binding configurations are further supported by the S 2p region that shows two distinct S 2p peaks. All peaks were fitted with a GL(30) function, and peak area ratio and spin-orbit splitting were constrained. The same full width at half maxima (FWHM) is used for peak doublets for both peaks.

Samples	$[Mo_3S_{13}]^{2-}$	$[Mo_3S_4]^{4+}$
1	30.97	6.45
2	15.92	5.97
3	30.25	6.93
4	30.23	5.10
5	33.74	6.04

Table S1 – Thickness of five different samples as measured by the profilometer (Dektac, Bruker), measuring the step difference between FTO and catalyst.

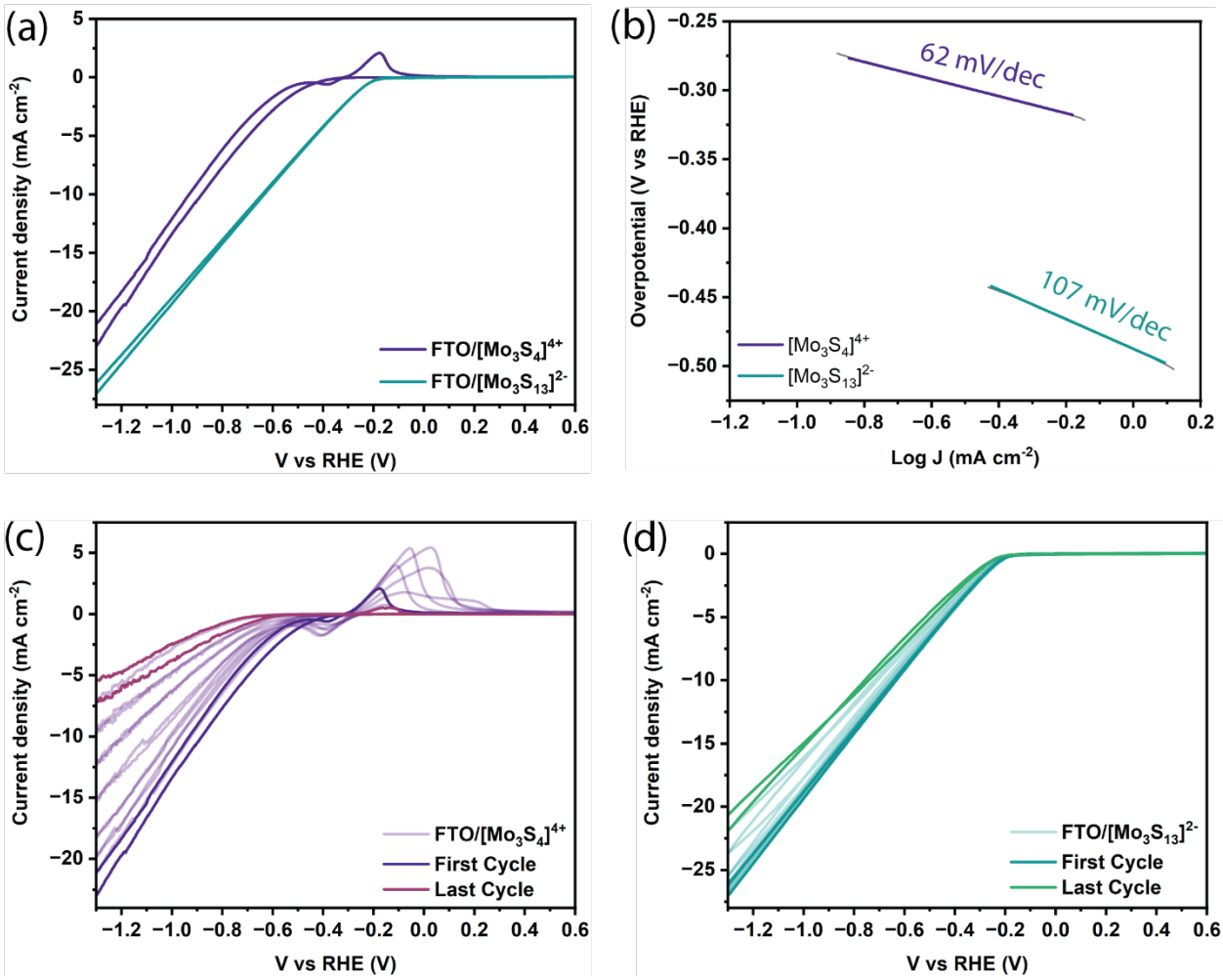

Figure S1 – (a) Dark CV measurements of $[Mo_3S_4]^{4+}$ and $[Mo_3S_{13}]^{2-}$ only on an FTO substrate (b) Tafel plots of $[Mo_3S_4]^{4+}$ and $[Mo_3S_{13}]^{2-}$an FTO substrate, IR drop corrected (c) performance of $[Mo_3S_4]^{4+}$ over 10 cycles (d) performance of $[Mo_3S_{13}]^{2-}$ over 10 cycles.

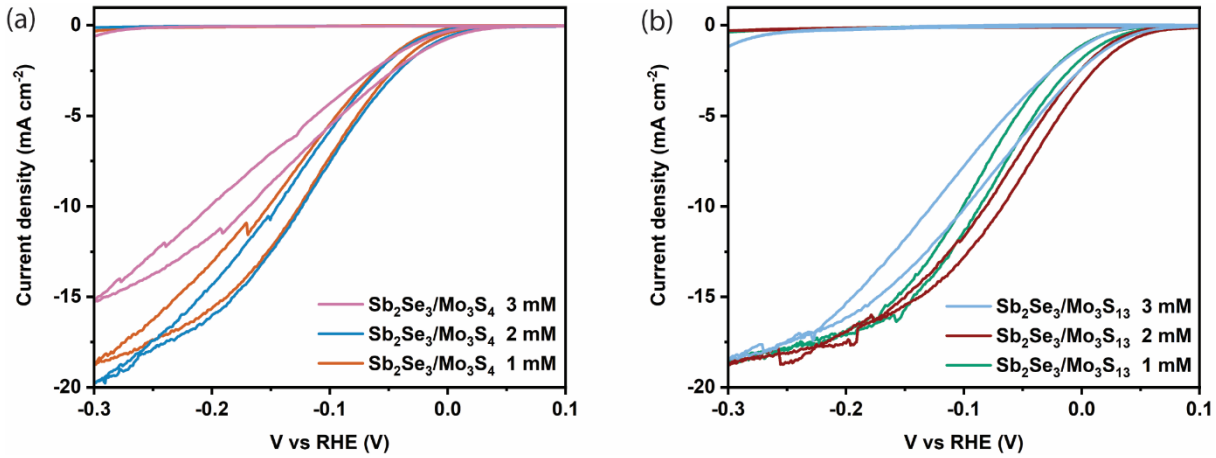

Figure S2 – (a) Cyclic voltammetry measurements of Sb_2Se_3 + $[Mo_3S_4]^{4+}$ samples at various concentrations at 1 sun illumination and in the dark (b) Cyclic voltammetry measurements of Sb_2Se_3 + $[Mo_3S_{13}]^{2-}$ samples at various concentrations at 1 sun illumination and in the dark.

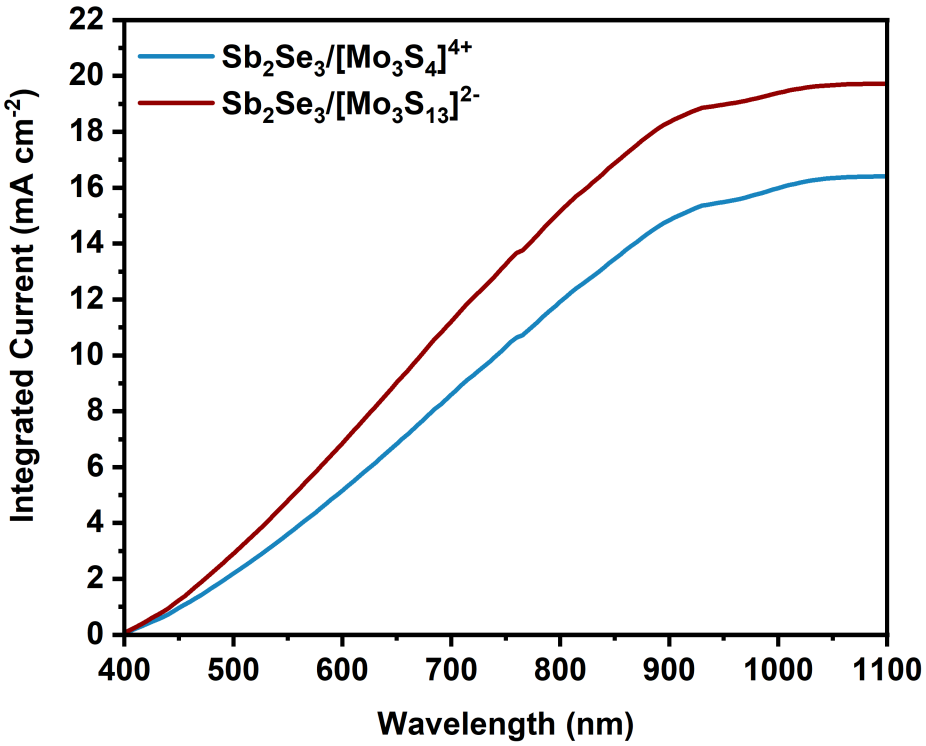

Figure S3 – Integrated photocurrents (mA cm^{-2}) based on the IPCE measurements in Fig 2b and under AM 1.5 G (100 mW cm^{-2}) simulated solar irradiation.

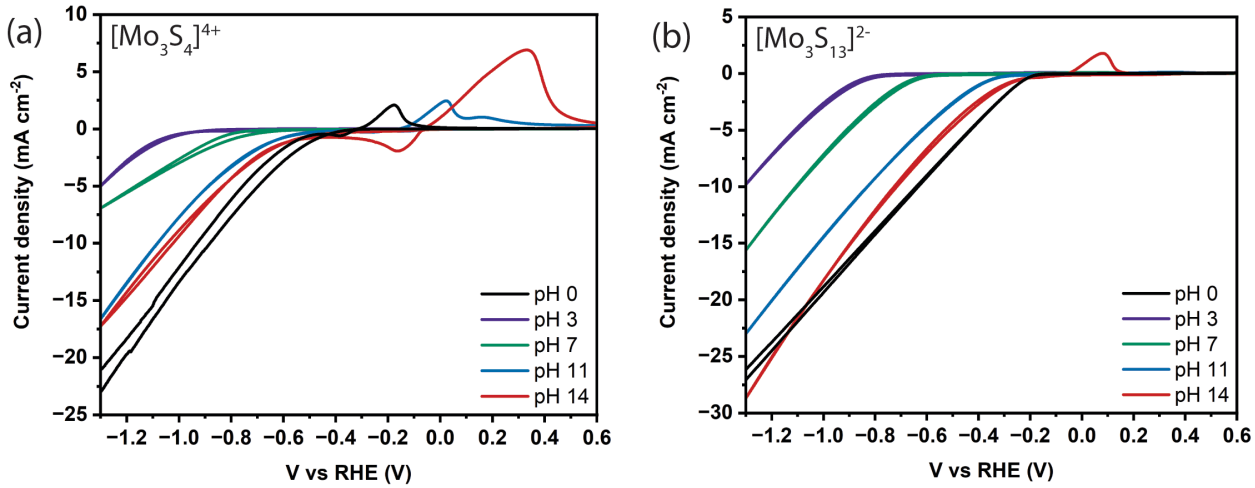

Figure S4 – (a) Cyclic voltammetry measurements of FTO + $[Mo_3S_4]^{4+}$ samples in different pH environments (b) Cyclic voltammetry measurements of FTO + $[Mo_3S_{13}]^{2-}$ samples in different pH environments.

$[Mo_3S_4]^{4+}$	S1	S2	S3	Average ± STD
H_2 (mol)	$2.13 \cdot 10^{-6}$	$1.06 \cdot 10^{-6}$	$1.43 \cdot 10^{-7}$	
Q_{el}/ C	0.403	0.219	0.0401	
FE (%)	102	93	69	88 ± 17

Table S2 – Measured and calculated values for $[Mo_3S_4]^{4+}S_4$ after applying –0.2 V versus RHE under 1 sun illumination for 10 min

$[Mo_3S_{13}]^{2-}$	S1	S2	S3	Average ± STD
H_2 (mol)	$1.61 \cdot 10^{-5}$	$2.06 \cdot 10^{-5}$	$6.08 \cdot 10^{-6}$	
Q_{el} (C)	3.20	3.60	1.15	
FE (%)	97	111	102	103 ± 7

Table S3 – Measured and calculated values for $[Mo_3S_{13}]^{2-}$ after applying –0.2 V versus RHE under 1 sun illumination for 10 min

	$[Mo_3S_{13}]^{2-}$		$[Mo_3S_4]^{4+}$	
t/min	**mol H_2**	**FE%**	**mol H_2**	**FE%**
1	$8.74 \cdot 10^{-7}$	55	$8.14 \cdot 10^{-8}$	9
5	$7.65 \cdot 10^{-6}$	98	$6.29 \cdot 10^{-7}$	21
10	$2.06 \cdot 10^{-5}$	110	$1.06 \cdot 10^{-6}$	93
20	$3.03 \cdot 10^{-5}$	80	$1.39 \cdot 10^{-6}$	112
30	$3.86 \cdot 10^{-5}$	102	-	-
30	$3.03 \cdot 10^{-5}$	80	-	-

Table S4 – Moles of hydrogen and faradaic efficiency of representative samples at different times (time is cumulative, e.g. $[Mo_3S_{13}]^{2-}$ the sample was measured for 96 minutes in total) at –0.2 V versus RHE under 1 sun illumination.

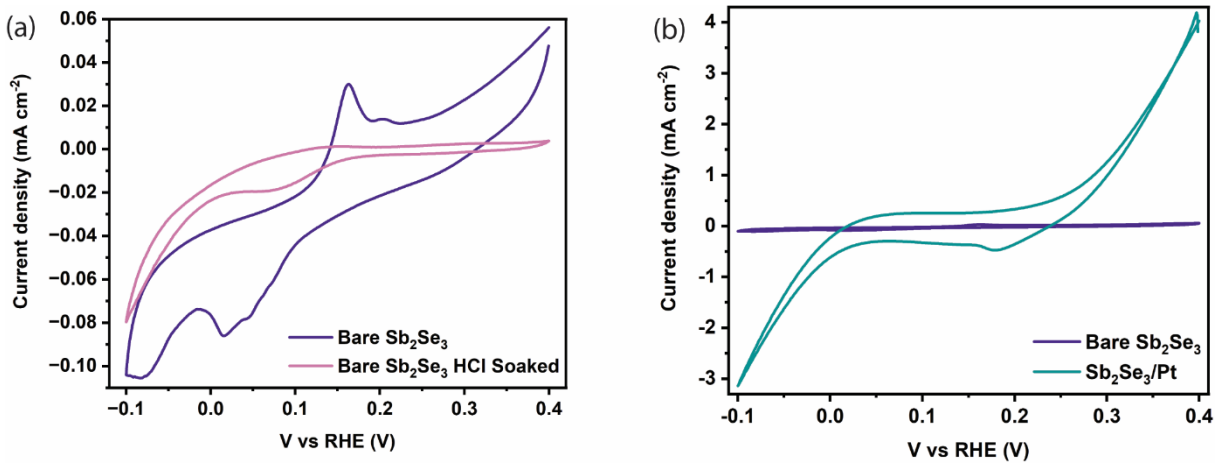

Figure S5 – (a) Cyclic voltammetry measurements of a bare Sb_2Se_3 sample and an Sb_2Se_3 sample soaked in HCl for 12 hours at 1 sun illumination with light chopping. (b) Cyclic voltammetry measurements of a bare Sb_2Se_3 sample and an Sb_2Se_3 sample with 2 nm of Pt as a catalyst at 1 sun illumination with light chopping.

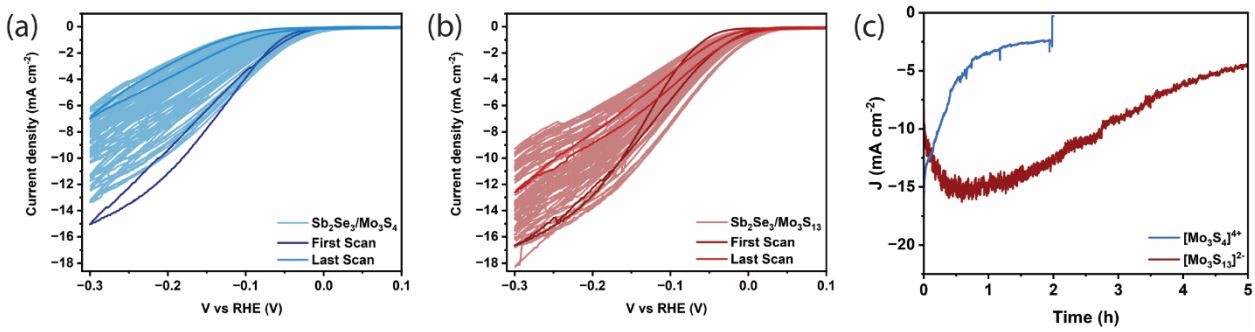

Figure S6 – (a) Cyclic voltammetry measurements of a Sb_2Se_3 + $[Mo_3S_4]^{4+}$ sample for 60 cycles at 1 sun illumination (10 mV s^{-1} equating to 80 minutes). (b) Cyclic voltammetry measurements of a Sb_2Se_3 + $[Mo_3S_{13}]^{2-}$ sample for 60 cycles at 1 sun illumination (10 mV s^{-1} equating to 80 minutes) (c) Chronoamprometric measurements of Sb_2Se_3 + $[Mo_3S_4]^{4+}$ and Sb_2Se_3 + $[Mo_3S_{13}]^{2-}$ at 1 sun illumination.

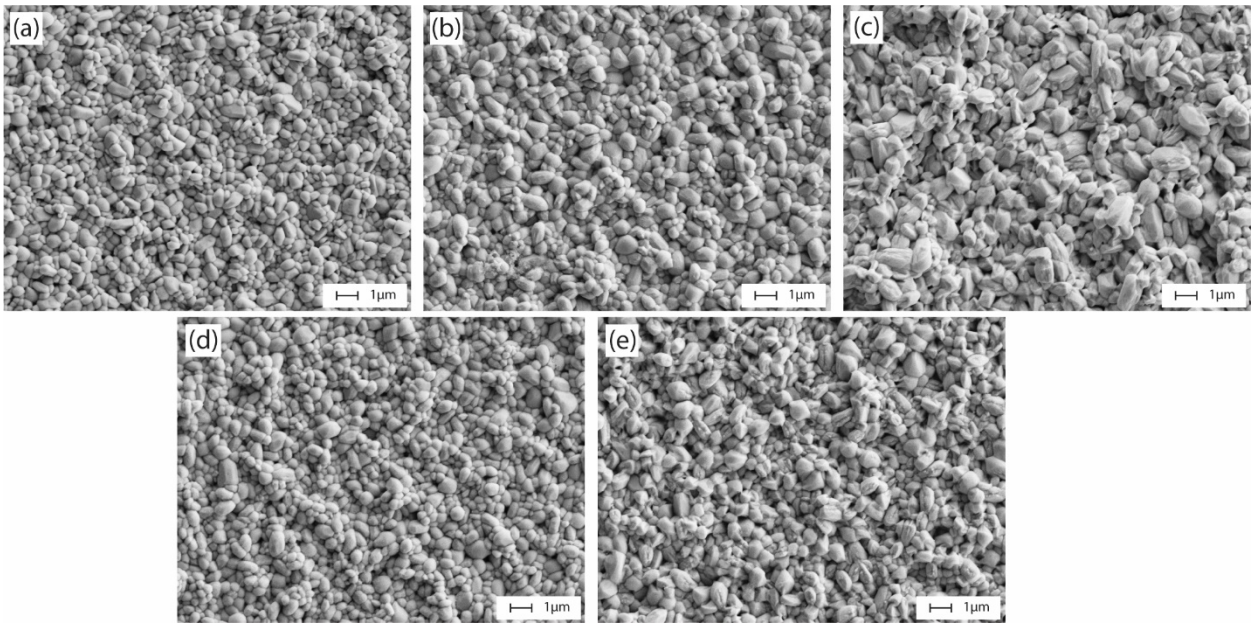

Figure S7 – (a) Top view SEM image of a typical untreated Sb_2Se_3 sample (b) Top view SEM images of a typical Sb_2Se_3 + $[Mo_3S_4]^{4+}$ sample (c) Top view SEM images of a typical Sb_2Se_3 + $[Mo_3S_4]^{4+}$ sample after PEC measurements (d) Top view SEM images of a typical Sb_2Se_3 + $[Mo_3S_{13}]^{2-}$ sample (e) Top view SEM images of a typical Sb_2Se_3 + $[Mo_3S_{13}]^{2-}$ sample after PEC measurements.

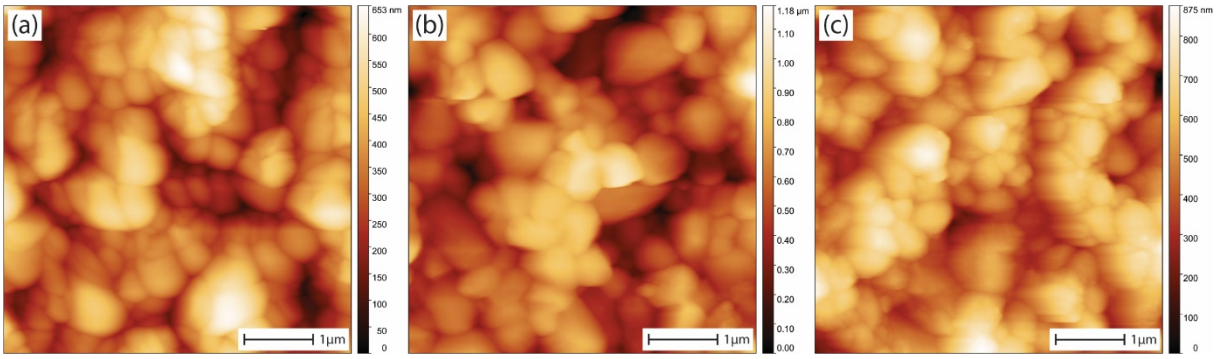

Figure S8 – (a) AFM image of a typical untreated Sb_2Se_3 sample. (b) AFM images of a typical Sb_2Se_3 + $[Mo_3S_4]^{4+}$ sample. (c) AFM images of a typical Sb_2Se_3 + $[Mo_3S_{13}]^{2-}$ sample.

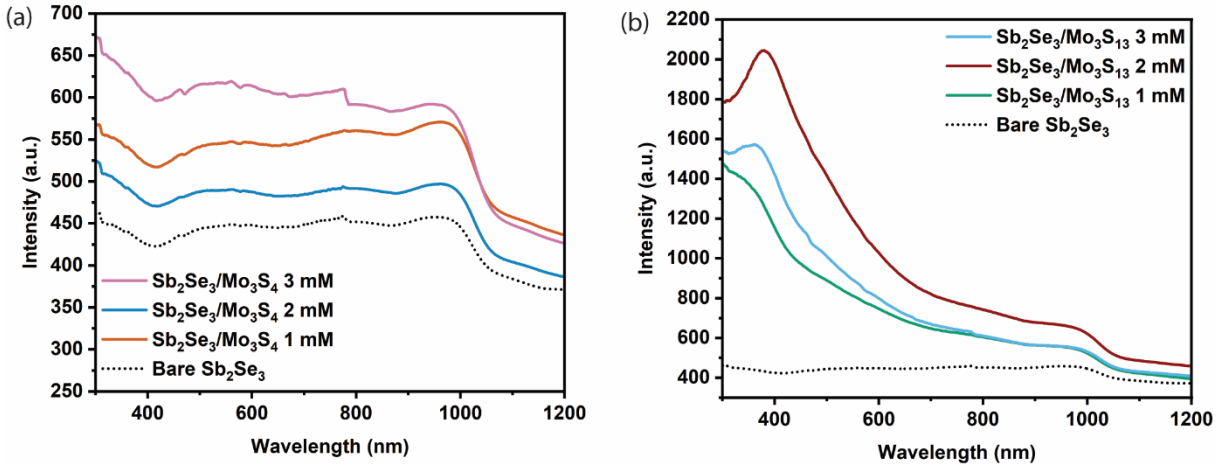

Figure S9 – (a) UV-Vis-NIR DRS of bare Sb_2Se_3 and Sb_2Se_3 + $[Mo_3S_4]^{4+}$ samples at three different concentrations of catalyst deposition solution, 1 mM, 2 mM, 3 mM. (b) Diffuse reflectance spectra of bare Sb_2Se_3 and Sb_2Se_3 + $[Mo_3S_{13}]^{2-}$ samples at three different concentrations of catalyst deposition solution, 1 mM, 2 mM, 3 mM.

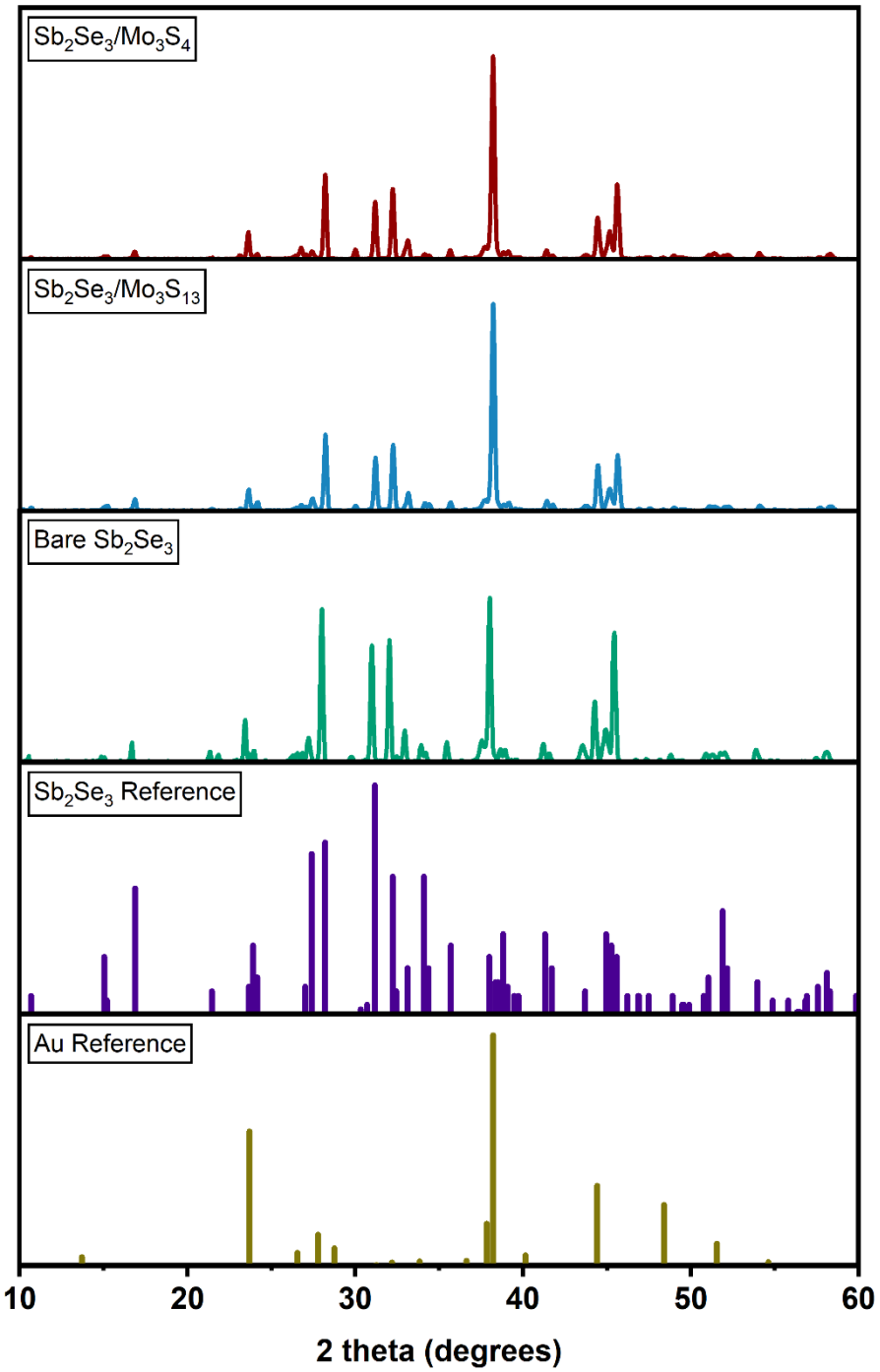

Figure S10 – XRD patterns of bare Sb_2Se_3, Sb_2Se_3 + $[Mo_3S_4]^{4+}$ and Sb_2Se_3 + $[Mo_3S_{13}]^{2-}$ compared to the orthorhombic phase of Sb_2Se_3 and Au reference cards (JCPDS 15-0861 and JCPDS 04-0784 respectively).

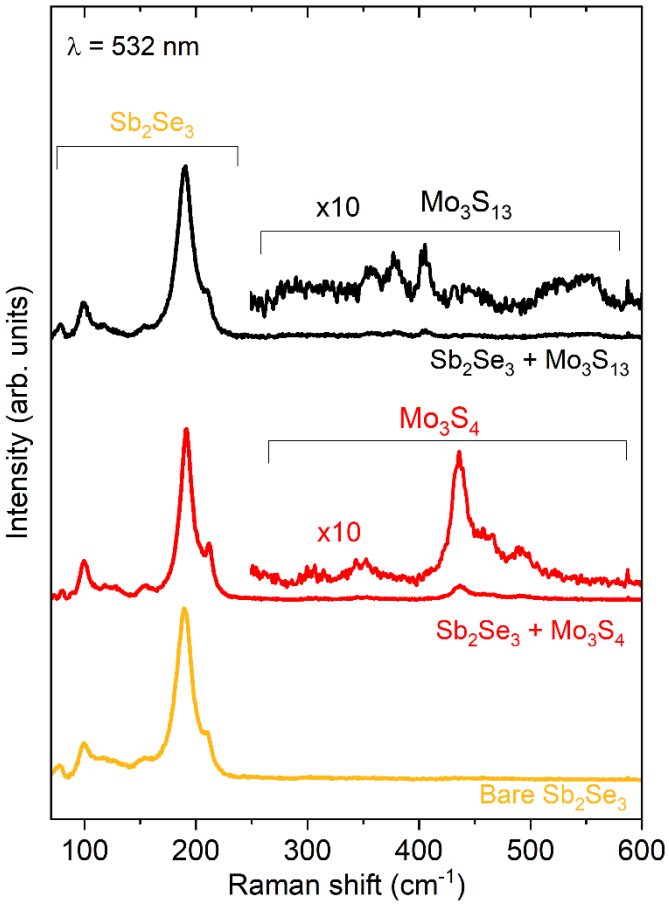

Figure S11 – Raman spectra of a typical bare Sb_2Se_3 sample, Sb_2Se_3 + $[Mo_3S_4]^{4+}$ and Sb_2Se_3 + $[Mo_3S_{13}]^{2-}$ after PEC measurements at the laser excitation wavelengths of 532 nm.

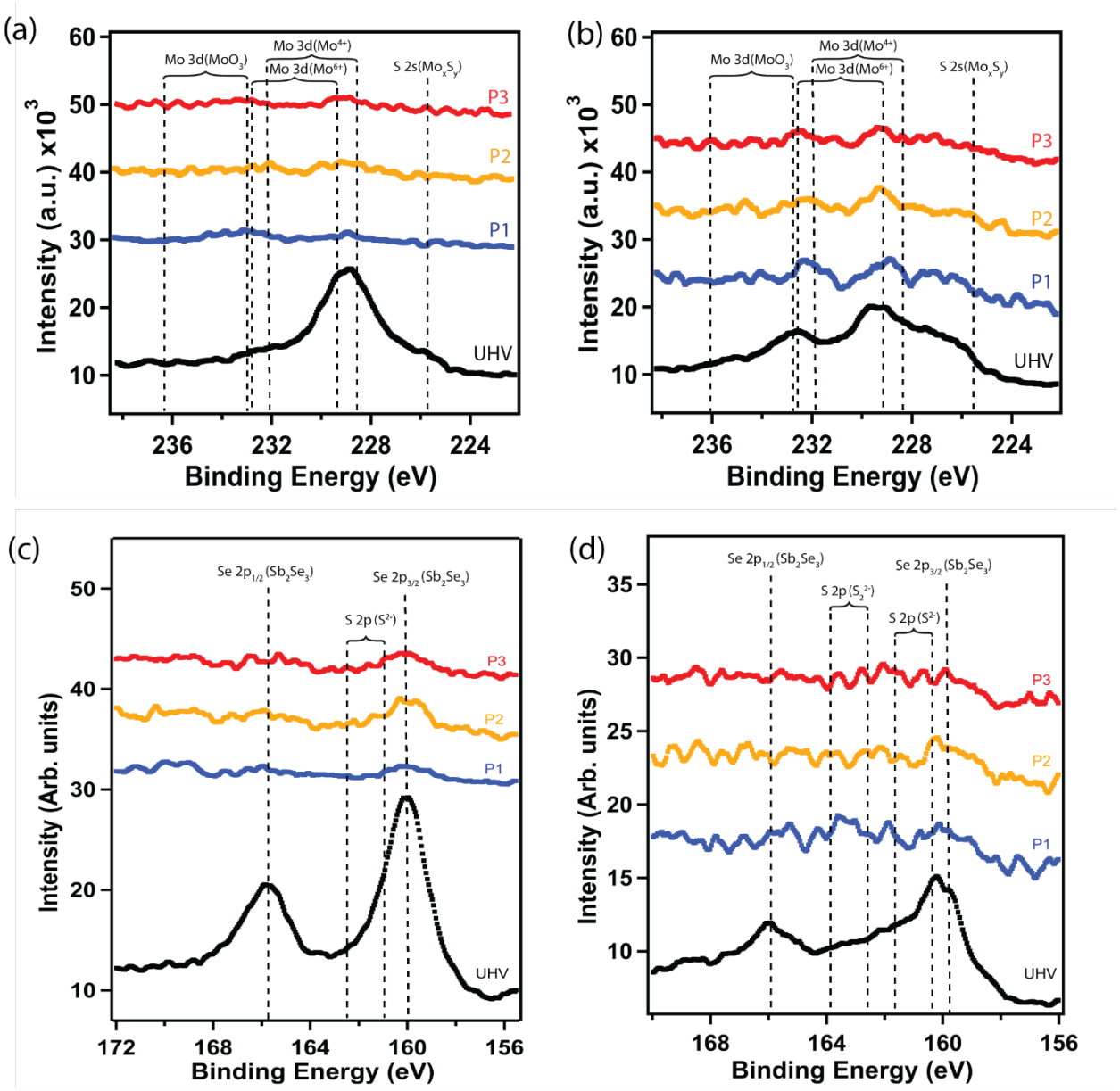

Figure S12 – NAPXPS measurements at a potential before onset (P1 - blue), at a potential around onset (P2 - orange) and at a potential after onset (P3 - red) and at ultra-high vacuum (UHV - black) (a) Mo 3d + S 2s spectrum of Sb_2Se_3 with $[Mo_3S_4]^{4+}$ catalyst (b) Mo 3d + S 2s spectrum of Sb_2Se_3 with $[Mo_3S_{13}]^{2-}$ catalyst (c) Se 3d spectrum of Sb_2Se_3 with $[Mo_3S_4]^{4+}$ catalyst (b) Se 3d spectrum of Sb_2Se_3 with $[Mo_3S_{13}]^{2-}$ catalyst. An SG 15 function was used to smooth the raw data and the dashed reference lines were extracted from NIST database.[7]

To understand the mechanism of action of the photoabsorber materials and the co-catalyst under realistic conditions such as applied bias, under illumination and in an electrolyte solution, near ambient pressure X-ray photoelectron spectroscopy (NAPXPS) can be utilized. Operating with tender X-rays (~4000 eV), this technique investigates the solid-liquid interface at pressure levels of a few millibars, with the differentially pumped electron analyzer withstanding room-temperature water vapor pressure inside the analysis chamber. Samples with amorphous molybdenum sulfide were highly hydrophilic, stabilizing a thick water film (thickness above 40 nm), which made studies of the solid-liquid interface with NAPXPS impossible. NAPXPS observations deemed the molybdenum sulfide cluster samples suitable, given their stability and minimal hydrophilicity. NAPXPS measurements were designed not only to understand the catalysts' behavior on the surface but also to investigate the charge carrier dynamics of Sb_2Se_3 films through surface photovoltage, which manifests as a change in binding energy. However, no discernible effects or changes were observed at different potentials and between dark and illuminated conditions. Nevertheless, NAPXPS provided valuable insights into the stability of the molybdenum sulfide clusters as catalysts. The NAPXPS endstation at the Swiss Light Source (SLS) at the Paul Scherer Institute (PSI) has a chamber capable of operating up to 30 mbar.[8] In this endstation, it is possible to position a beaker containing an aqueous electrolyte solution just below the inlet cone of the analyzer. After being immersed in the electrolyte, the sample can be set up in a standard three-electrode arrangement to perform in-situ cyclic voltammetry. By employing appropriate reduction-oxidation cycles through electrochemical processes, well-defined surface preparations can be accomplished, resulting in atomically pristine surfaces. The sample can be moved in front of the analyzer cone, maintaining a short distance (600 µm) from the orifice leading to the differentially-pumped lens optics. In instances involving hydrophilic surfaces, sustaining a continuous water film with a few tens of nanometers thickness is feasible, which allows probing of the liquid-solid interface when using tender X-rays (3-5 keV).[9]

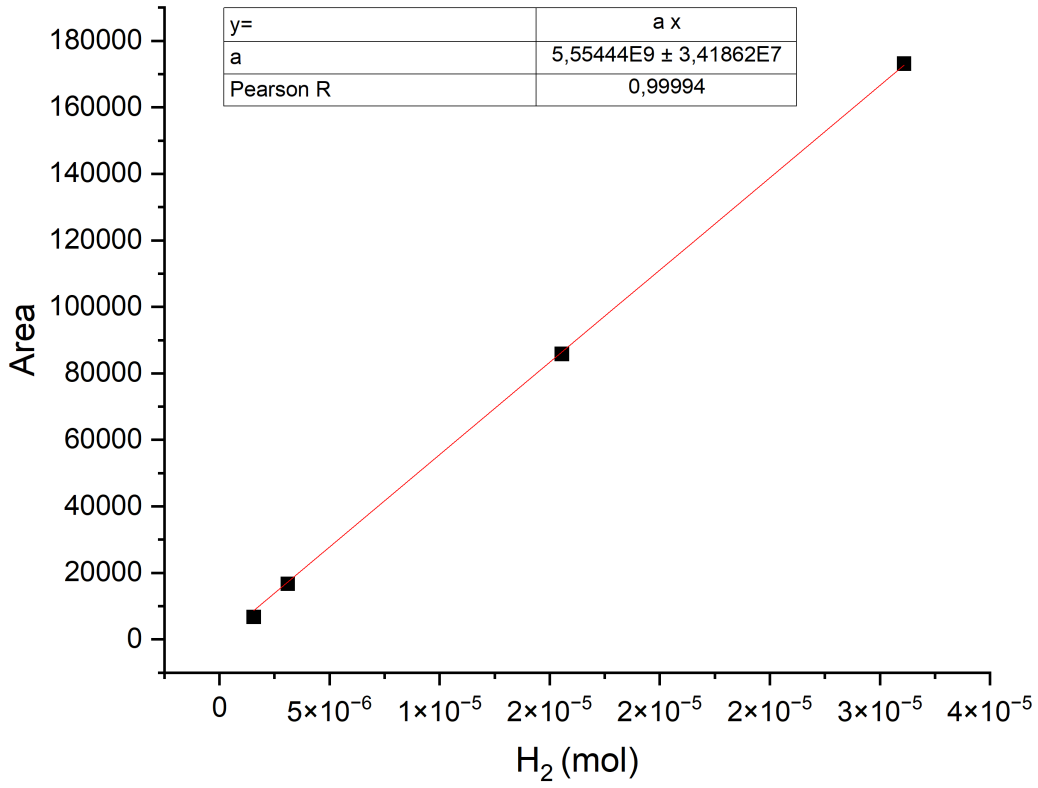

Figure S13 – Calibration curve for the electrochemical hydrogen production and the gas chromatography peak area, assuming a 100% FE for the HER on Pt. The resulting slope of y= a*x is a= $5.55 \cdot 10^9$ (after forcing intercept).

I applied (mA)	**t (min)**	**Q_{el} (C)**	**N_{H2} (mol)**	**Area**
– 0.5	10	0.300	1.56E-06	6779
– 1	10	0.600	3.11E-06	16744
– 5	10	3.00	1.56E-05	85811
– 10	10	6.00	3.11E-05	173156

Table S5 – Data For Calibration Curve

The calibration was performed by applying galvanostatic currents (–0.5, 1, 5, and 10 mA) to a Pt wire working electrode and a Pt counter electrode in a two-electrode setup, assuming a faradaic efficiency of 100% for HER on Pt. A calibration curve was determined by plotting the peak area measured with gas chromatography versus the produced amount of hydrogen (mol). The produced amount of hydrogen N (mol) was determined via:

$$\mathbf{N} = \frac{\mathbf{Q_{el}}}{\boldsymbol{Fn}} \qquad \textbf{(eq. 1)}$$

With Q_{el} = charged flowed during chronopotentiometry (C), n = 2 (number of electrons), F = Faraday constant = 96485.33 (C mol^{-1}). The samples were irradiated with one sun with a white LED, and a potential of –0.2 V versus RHE (chronoamperometry, CA) was applied for specified times. Afterwards, the hydrogen gas was measured. Inserting the measured peak area into the calibration curve gives the hydrogen produced in mol (N).

$$\mathbf{Q = nFN} \qquad \textbf{(eq. 2)}$$

With n = 2 (number of electrons), F = Faraday constant = 96485.33 C mol^{-1}, N produced mol of H_2. Finally, faradaic efficiency was calculated using the equation below:

$$\mathbf{FE} = \frac{\mathbf{Q}}{\mathbf{Q_{el}}} \times \mathbf{100} \qquad \textbf{(eq. 3)}$$

Crystal Data

Experimental

Single crystal X-ray diffraction data were collected at 160.0(1) K on a Rigaku OD Supernova/Atlas diffractometer using the copper X-ray radiation (λ = 1.54184 Å) from a dual wavelength X-ray source and an Oxford Instruments Cryojet XL cooler. The selected suitable single crystal was mounted using polybutene oil on a flexible loop fixed on a goniometer head and immediately transferred to the diffractometer. Pre-experiment, data collection, data reduction and analytical absorption correction.[10] were performed with the program suite CrysAlisPro.[11] Using Olex2,[12] the structure was solved with the SHELXt.[13] small molecule structure solution program and refined with the SHELXL2018/3 program package[14] by full-matrix least-squares minimization on F^2. PLATON[15] was used to check the result of the X-ray analysis. For more details about the data collection and refinement parameters, see the CIF files.

Crystal Data of $[Mo_3S_4(H_2O)_9](OTs)_4$

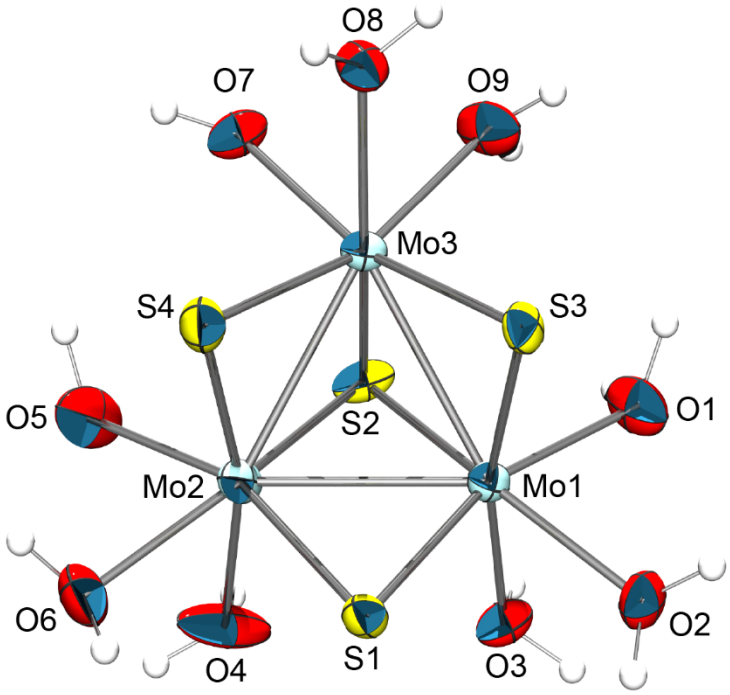

Figure S12 – Displacement ellipsoids of $[Mo_3S_4(H_2O)_9](OTs)_4$. Counter ions and solvent molecules are omitted for clarity, thermal ellipsoids represent 50% probability. Single crystals were obtained after anion exchange with p-toluenesulfonate (OTs) by cooling of a concentrateted solution at −20 °C.[1,2]

Special features

All counterions $C_7H_7O_3S^-$ are partially or completely disordered over two sets of positions. The main species cocrystallized with solvent molecules of water.

Empirical formula	$C_{28}H_{65.72}Mo_3O_{30.86}S_8$
Formula weight	1440.58
Temperature/K	160.0(1)
Crystal system	triclinic
Space group	P-1
a/Å	11.9671(2)
b/Å	15.1770(3)
c/Å	16.5425(3)
α/°	101.825(2)
β/°	96.063(2)
γ/°	109.273(2)
Volume/Å^3	2726.71(9)
Z	2
ρ_{calc}g/cm^3	1.755
μ/mm^{-1}	9.205
F(000)	1469.0
Crystal size/mm^3	0.24 × 0.11 × 0.03
Radiation	Cu Kα (λ = 1.54184)
2Θ range for data collection/°	5.556 to 149.006
Index ranges	$-14 \leq h \leq 14$, $-18 \leq k \leq 18$, $-20 \leq l \leq 20$
Reflections collected	55138
Independent reflections	11106 [R_{int} = 0.0309, R_{sigma} = 0.0204]

Data/restraints/parameters	11106/1907/971
Goodness-of-fit on F^2	1.087
Final R indexes [I>=2σ (I)]	R_1 = 0.0517, wR_2 = 0.1205
Final R indexes [all data]	R_1 = 0.0536, wR_2 = 0.1217
Largest diff. peak/hole / e $Å^{-3}$	1.66/−1.38

Table S6 – Crystal Data and Structure Refinement for $[Mo_3S_4(H_2O)_9](OTs)_4$

Crystal Data for $C_{28}H_{65.72}Mo_3O_{30.86}S_8$ (M =1440.58 g/mol): triclinic, space group P-1 (no. 2), a = 11.9671(2) Å, b = 15.1770(3) Å, c = 16.5425(3) Å, α = 101.825(2)°, β = 96.063(2)°, γ = 109.273(2)°, V = 2726.71(9) $Å^3$, Z = 2, T = 160.0(1) K, μ(Cu Kα) = 9.205 mm^{-1}, Dcalc = 1.755 g/cm^3, 55138 reflections measured (5.556° ≤ 2Θ ≤ 149.006°), 11106 unique (R_{int} = 0.0309, R_{sigma} = 0.0204) which were used in all calculations. The final R_1 was 0.0517 (I > 2σ(I)) and wR_2 was 0.1217 (all data).

Crystal Data of $(NH_4)_2[Mo_3S_{13}]$

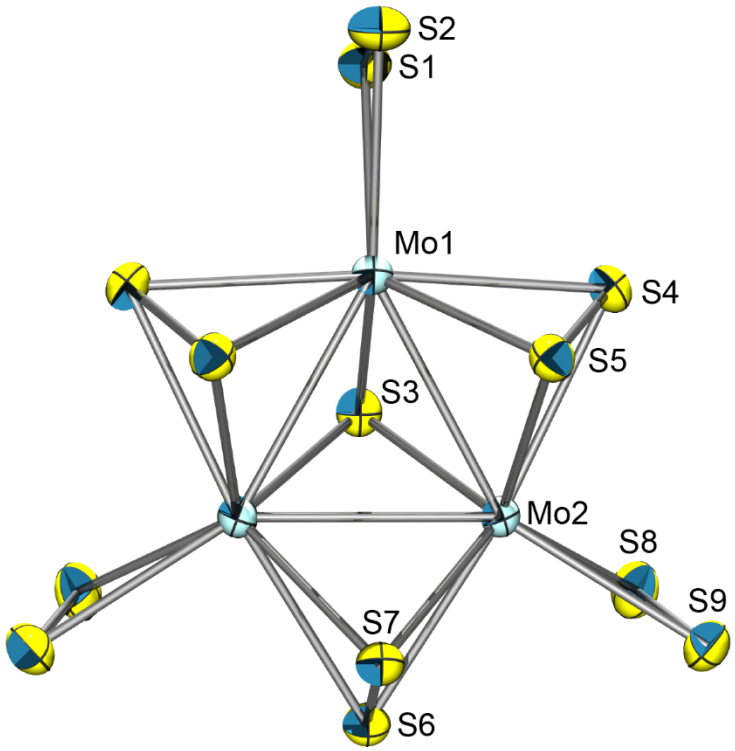

Figure S13 – Displacement ellipsoids of $(NH_4)_2[Mo_3S_{13}]$. Counter ions and solvent molecules are omitted for clarity, thermal ellipsoids represent 50% probability. Single crystals were were picked directly from the obtained crystalline solid after synthesis.[3]

Special features

In the asymmetric unit the $[Mo_3S_{13}]^{2-}$ ion is located on a mirror plane. Only half of the molecule was refined, while the second part being reproduced by a symmetry operation.

Empirical formula	$H_{9.62}Mo_3N_2O_{0.81}S_{13}$
Formula weight	755.28
Temperature/K	160.0(1)
Crystal system	monoclinic
Space group	Cm
a/Å	11.3842(3)
b/Å	16.5251(3)
c/Å	5.68090(10)
α/°	90
β/°	116.354(4)
γ/°	90
Volume/Å^3	957.65(5)
Z	2
ρ_{calc}g/cm^3	2.619
μ/mm^{-1}	29.031
F(000)	728.0
Crystal size/mm^3	0.05 × 0.03 × 0.01
Radiation	Cu Kα (λ = 1.54184)
2Θ range for data collection/°	10.19 to 148.97
Index ranges	$-13 \leq h \leq 14$, $-20 \leq k \leq 20$, $-7 \leq l \leq 7$
Reflections collected	10314
Independent reflections	1946 [R_{int} = 0.0335, R_{sigma} = 0.0223]

Data/restraints/parameters	1946/6/104
Goodness-of-fit on F^2	1.054
Final R indexes [I>=2σ (I)]	R_1 = 0.0212, wR_2 = 0.0539
Final R indexes [all data]	R_1 = 0.0216, wR_2 = 0.0542
Largest diff. peak/hole / e $Å^{-3}$	1.11/−0.65
Flack parameter	−0.022(11)

Table S7 – Crystal Data and Structure Refinement for $(NH_4)_2[Mo_3S_{13}]$.

Crystal Data for $H_{9.62}Mo_3N_2O_{0.81}S_{13}$ (M =755.28 g/mol): monoclinic, space group Cm (no. 8), a = 11.3842(3) Å, b = 16.5251(3) Å, c = 5.68090(10) Å, β = 116.354(4)°, V = 957.65(5) $Å^3$, Z = 2, T = 160.0(1) K, μ(Cu Kα) = 29.031 mm^{-1}, Dcalc = 2.619 g/cm^3, 10314 reflections measured (10.19° ≤ 2Θ ≤ 148.97°), 1946 unique (R_{int} = 0.0335, R_{sigma} = 0.0223) which were used in all calculations. The final R_1 was 0.0212 (I > 2σ(I)) and wR_2 was 0.0542 (all data).

Deposition numbers 2320550 (for S12) and 2320551 (for S13) contain the supplementary crystallographic data for this paper. These data are provided free of charge by the joint Cambridge Crystallographic Data Centre and Fachinformationszentrum Karlsruhe Access Structures service.

(1) Dimitri Coucouvanis. *Inorganic Syntheses*; Coucouvanis, D., Ed.; Inorganic Syntheses; Wiley, 2002; Vol. 33. https://doi.org/10.1002/0471224502.

(2) Shibahara, T.; Yamasaki, M.; Sakane, G.; Minami, K.; Yabuki, T.; Ichimura, A. Syntheses and Electrochemistry of Incomplete Cubane-Type Clusters with M3S4 Cores (M = Molybdenum, Tungsten). X-Ray Structures of [W3S4(H2O)9](CH3C6H4SO3)4.Cntdot.9H2O, Na2[W3S4(Hnta)3].Cntdot.5H2O, and (BpyH)5[W3S4(NCS)9].Cntdot.3H2O. *Inorg Chem* **1992**, *31* (4), 640–647. https://doi.org/10.1021/ic00030a022.

(3) Dave, M.; Rajagopal, A.; Damm-Ruttensperger, M.; Schwarz, B.; Nägele, F.; Daccache, L.; Fantauzzi, D.; Jacob, T.; Streb, C. Understanding Homogeneous Hydrogen Evolution Reactivity and Deactivation Pathways of Molecular Molybdenum Sulfide Catalysts. *Sustain Energy Fuels* **2018**, *2* (5), 1020–1026. https://doi.org/10.1039/c7se00599g.

(4) Adams, P.; Creazzo, F.; Moehl, T.; Crockett, R.; Zeng, P.; Novotny, Z.; Luber, S.; Yang, W.; Tilley, S. D. Solution Phase Treatments of Sb 2 Se 3 Heterojunction Photocathodes for Improved Water Splitting Performance. *J Mater Chem A Mater* **2023**, *11* (15), 8277–8284. https://doi.org/10.1039/D3TA00554B.

(5) Beerbom, M. M.; Lägel, B.; Cascio, A. J.; Doran, B. V.; Schlaf, R. Direct Comparison of Photoemission Spectroscopy and in Situ Kelvin Probe Work Function Measurements on Indium Tin Oxide Films. *J Electron Spectros Relat Phenomena* **2006**, *152* (1–2), 12–17. https://doi.org/10.1016/j.elspec.2006.02.001.

(6) Novotny, Z.; Aegerter, D.; Comini, N.; Tobler, B.; Artiglia, L.; Maier, U.; Moehl, T.; Fabbri, E.; Huthwelker, T.; Schmidt, T. J.; Ammann, M.; van Bokhoven, J. A.; Raabe, J.; Osterwalder, J. Probing the Solid–Liquid Interface with Tender x Rays: A New Ambient-Pressure x-Ray Photoelectron Spectroscopy Endstation at the Swiss Light Source. *Review of Scientific Instruments* **2020**, *91* (2), 023103. https://doi.org/10.1063/1.5128600.

(7) *NIST X-ray Photoelectron Spectroscopy Database*. https://srdata.nist.gov/xps/ (accessed 2024-05-30).

(8) Novotny, Z.; Aegerter, D.; Comini, N.; Tobler, B.; Artiglia, L.; Maier, U.; Moehl, T.; Fabbri, E.; Huthwelker, T.; Schmidt, T. J.; Ammann, M.; Van Bokhoven, J. A.; Raabe, J.; Osterwalder, J. Probing the Solid-Liquid Interface with Tender x Rays: A New Ambient-Pressure X-Ray Photoelectron Spectroscopy Endstation at the Swiss Light Source. *Review of Scientific Instruments* **2020**, *91* (2), 23103. https://doi.org/10.1063/1.5128600.

(9) Axnanda, S.; Crumlin, E. J.; Mao, B.; Rani, S.; Chang, R.; Karlsson, P. G.; Edwards, M. O. M.; Lundqvist, M.; Moberg, R.; Ross, P.; Hussain, Z.; Liu, Z. Using "Tender" X-Ray Ambient Pressure X-Ray Photoelectron Spectroscopy as A Direct Probe of Solid-Liquid Interface. *Sci Rep* **2015**, *5* (1), 1–12. https://doi.org/10.1038/srep09788.

(10) Clark, R. C.; Reid, J. S. The Analytical Calculation of Absorption in Multifaceted Crystals. *Acta Crystallographica Section A* **1995**, *51* (6), 887–897. https://doi.org/10.1107/S0108767395007367.

(11) *CrysAlisPro*; (version 1.171.43.97a), Rigaku Oxford Diffraction Ltd: Yarnton, Oxfordshire, England, 2023.

(12) Dolomanov, O. V.; Bourhis, L. J.; Gildea, R. J.; Howard, J. A. K.; Puschmann, H. OLEX2: A Complete Structure Solution, Refinement and Analysis Program. *J Appl Crystallogr* **2009**, *42* (2), 339–341. https://doi.org/10.1107/S0021889808042726.

(13) Sheldrick, G. M. SHELXT - Integrated Space-Group and Crystal-Structure Determination. *Acta Crystallogr A* **2015**, *71* (1), 3–8. https://doi.org/10.1107/S2053273314026370.

(14) Sheldrick, G. M. Crystal Structure Refinement with SHELXL. *Acta Crystallogr C Struct Chem* **2015**, *71* (1), 3–8. https://doi.org/10.1107/S2053229614024218.

(15) Spek, A. L. Structure Validation in Chemical Crystallography. *Acta Crystallogr D Biol Crystallogr* **2009**, *65* (2), 148–155. https://doi.org/10.1107/S090744490804362X.